Computing Metrics to Investigate Sex Differences in Brain Network Dynamics

Ben Griffin

St Cross College

University of Oxford

A thesis submitted for the degree of

M.Sc. in Mathematical Modelling and Scientific Computing

Trinity Term 2020

Acknowledgements

Abstract

Technological advances in brain imaging techniques have enabled neuroscientists to make new discoveries by applying modern graph theory tools to brain networks. This thesis investigates the structural organisation of the human brain by analysing data from the Human Connectome Project Young Adult study, where participants underwent a six minute resting-state magnetoencephalography (MEG) scan. Time-series data were divided into the six common frequency bands - theta (4–8 Hz), alpha (8–13 Hz), beta (13–30 Hz), low gamma (30–60 Hz), and high gamma (60–150 Hz) - and analysed independently using static and dynamic graph theoretical tools. Static modular analysis highlighted differences between community structures of networks of lower and higher frequencies. This difference supports the current understanding that brain processes occurring in lower frequency bands are based on a different brain structure from the cognitive functions in higher frequency bands. By applying a dynamic community detection algorithm and introducing four dynamic metrics, we highlighted how community assignment of the brain's regions of interest varies across time windows and frequency bands, with particular variation between the brain's intrinsic functional systems. Treating the networks of each time window as slices of a multislice network, global, local, and mesoscale distance metrics showed that the networks of the lower frequency bands tended to have larger distances between each other. Finally, dividing the subjects into 15 males and 15 females, our analysis suggested that dynamic topological properties were influenced by sex differences. The methodological approach developed in this work provides a framework to understand differences between male and female brains using recent mathematical and neuroscientific techniques. Future investigations will be able to apply this approach to improve our understanding of the brain and its cognitive functions.

Contents

Contents

List of Figures

List of Tables

Chapter 1

Introduction

1.1 Motivation

Network theory has gained prominence in recent years, with networks being used to represent complex social, biological, and technological systems [1, 2, 3]. In particular, neuroscientists have made advancements in their field by using networks to represent the human brain. By using nodes to represent regions of the brain and edges to represent connections between the nodes, researchers have been able to gain new insight into the brain's structural and functional organisation. This discipline, referred to as network neuroscience, has now become commonplace in research [4].

There had been much debate throughout the 19th century about whether the functionality of the brain is regional, with different areas being responsible for different functions, or whether the functionality is spread throughout the brain. In 1861, the neurologist Paul Broca provided evidence to support the former [5]. After examining a patient who was unable to speak, but otherwise displayed effective cognitive functionality, Broca located a lesion on the frontal lobe of the patient's brain. Due to the fact that the rest of the brain was healthy, this discovery supported his hypothesis that the frontal lobe region was responsible for producing speech. Since then, neurologists have been able to show that different regions of the brain are responsible for different functions. This regional functionality theory is one of the inspirations for viewing the brain as a network.

Network neuroscience has proven extremely effective in investigating previously unexplored ideas. Brain networks have been used to predict personality traits and performance on intelligence tests, as well as investigate neurological disorders. For example, Dubois et al. were able to use networks representing the brain to predict participants' openness to new experiences [6]. In addition to the idea of regional

functionality, neuroscientists began to realise that the connectivity between regions of the brain plays an important role. New brain imaging techniques, developed in the last few decades, have proven fundamental for examining this connectivity and helping to understand how regions of the brain interact.

Since being introduced in 1990, functional magnetic resonance imaging (fMRI) has been able to highlight regional, time-varying changes in brain structure by measuring the blood flow changes in different areas of the brain [7]. By determining which brain regions are active simultaneously, fMRI techniques are able to determine a 'functional connectivity' between the regions that can uncover new dynamic properties of the brain. For example, researchers have been able to show that patients with schizophrenia not only display differences in specific regions of the brain, but also in the connectivity of those regions [8, 9]. Neuroscientists hope that, in the future, this type of research may potentially enable earlier diagnosis of disorders. To further this investigation, it has been imperative to discover natural modules of the brain and examine the way these modules interact. This is done through community detection.

In network theory, one of the most important and recurring concepts is that of communities due to its wide ranging impact. For example, searching for communities in social networks has the potential to help prevent security threats including network corruption and computer viruses [10]. The concept rests on the idea that nodes of a network form close communities that are densely connected to each other, but sparsely connected to other communities in the network [11]. Detecting communities within networks can highlight some of the complex interactions between nodes [12], as well as shed light on the network's organisational principles. In the context of neurology, detecting communities enables us to examine the structural organisation of the brain.

In addition to revealing certain topological characteristics through static examination of the brain, community detection can also provide a dynamic viewpoint of how the brain changes over time. Is it known that the brain constantly adjusts its functional properties, with different regions working together differently depending on the brain's demands. Although particular attention has been paid to these changes while subjects complete prescribed tasks during an experiment [13, 14, 15], less research has focused on the dynamics of the brains of subjects in resting-state. However, it is worth considering the fact that if a subject has a disorder, then they have that disorder even when they are not completing a task. Additionally, Finn et al. were able to demonstrate individual differences in functional connectivity of subject brains, particularly while they were in their resting-state [16]. Therefore,

it is still imperative to analyse networks that represent the brains of subjects in resting-state.

In the same vein, significant attention has also been paid to discovering potential explanations or causes (i.e. structural and dynamical differences) of neurological diseases, by comparing the human brains of healthy volunteers and subjects with a pathological condition [17, 18]. One goal of these studies is to understand why some brain disorders are more prominent in one sex than the other [19].

Brain structure is similar between sexes. However, there are specific morphological and functional brain differences between males and females [20, 21], with certain features being more common in one sex than the other [22]. These brain differences may help explain a wide range of behavioural and clinical conditions that manifest differently in men and women (e.g. chronic pain, multiple sclerosis, fibromyalgia) [23, 24].

Discovering these differences has the potential to provide earlier diagnosis of diseases and find predictors of treatment outcome. Therefore, integrating sex as a variable into biomedical research is of significant interest [25]. The main aim of this thesis is to contribute to these largely unaddressed areas, by examining the brain networks of healthy male and female subjects while in their resting state.

1.2 Static and dynamic community detection in neuroscience

A plethora of neuroscientific studies have investigated how brain features may change between individuals (patient vs control) and in experimental conditions. By taking a snapshot of the brain at a single point in time, or its mean over a period of time, studies have been able to highlight distinct differences between subjects using static modular analysis. For example, studies have demonstrated differences in modularity between a control group and patients with childhood-onset schizophrenia [17], and subjects trained to complete memory-driven tasks [13]. Additionally, Meunier et al. [26] reported that brains of both young and older people showed significantly different levels of modularity compared to random networks.

A few recent studies have used a dynamic approach to assess brain networks, focusing on communities of the networks over a certain period of time. Finc et al. [13] supported their static analysis with dynamic modular analysis, showing that nodes from different cortical systems have a tendency to remain in the same communities as subjects are trained to complete memory tasks. Additionally, dynamic modular

analysis has been used to show that brain nodes change their allegiance to different brain systems through time while viewing meaningful images [27], performing a variety of tasks [14], and during learning [15].

The literature that has applied methods from static [17, 26] and dynamic [13, 14, 15] modular analyses has primarily used data obtained from fMRI scans. From brain imaging data, a graph can be created using any one of a number of measures of association between brain regions, including the statistical dependence between neurophysiological signals. In fMRI, the most common approach measures the correlation coefficient (Pearson correlation), such that brain regions with correlated activity are said to be functionally connected. It is worth noting that functional connectivity represents a statistical relationship between a pair of nodes and, therefore, a correlation does not necessarily imply that one node is causing activity in the other, or that the nodes share a direct anatomical connection.

Data from fMRI provide a good spatial resolution but have a very low temporal resolution (i.e. several seconds), which can be an issue when investigating dynamic temporal changes in the brain. Electroencephalography (EEG) is another method to record electrical activity of the brain with a very good temporal resolution, but with a low spatial resolution (several brain imaging methods and their temporal and spatial resolutions are presented in Figure 1.1).
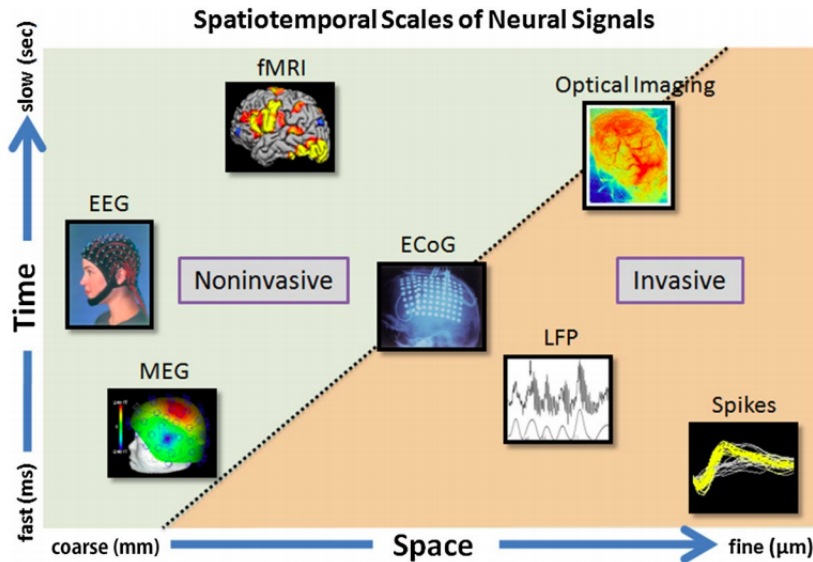
Figure 1.1: Spatial and temporal resolutions of the most widely used functional brain imaging techniques. Image obtained from [28].

Magnetoencephalography (MEG) is the newest, most advanced method that combines the advantages of both fMRI and EEG. MEG records the magnetic field

generated by the electrical activity of neurons, allowing the measurement of ongoing brain activity on a millisecond-by-millisecond basis.

Kabbara et al. [29] applied dynamic analysis on both resting EEG and MEG data, and were able to show a correlation between brain dynamics and personality traits.

In this thesis, we choose to use the most advanced method in the field and work on data obtained from MEG imaging methods in order to gain a deeper insight into the dynamics of the brain. Due to the improved temporal resolution that MEG data provides, we can easily disassociate functional bands of different frequencies, or *frequency bands*.

1.3 Distance metrics for comparing graphs

Recent research has also looked at applying distance metrics from graph theory to brain networks. The choice of metric used to analyse the dynamics of the brain is an important one, with an appropriate choice helping to identify similar graph-states. Additionally, distance metrics enable elementary but effective statistical analysis to be performed. For example, comparing pairwise distances or defining a mean, median, and variance of data follows naturally from an appropriate metric. This is particularly useful for identifying sex differences in the dynamics of the brain.

Donnat et al. [30] introduced several metrics to calculate a distance between two graphs and then used the metrics to analyse fMRI data of cocaine-dependent patients. Their analysis was able to highlight a correlation between cocaine-dependency and differences between brain connectomes.

1.4 Project goals and overview

The objectives of the present work are to:

(i) apply static and dynamic graph analyses to investigate the intrinsic functional systems of the brain at different frequencies;

(ii) compare and contrast the specificity, reliability, and robustness of distance metrics for analysing brain networks;

(iii) investigate potential structural and dynamical differences between male and female brains.

In Chapter 2, we discuss the method used to preprocess the data of subjects selected for our analysis, which produces functional connectivity matrices that are then converted to adjacency matrices. After determining communities in the subjects' networks, tools from static modular analysis are used to compare the quality of partitions and analyse the differences in community structure of the networks of each frequency band.

Chapter 3 investigates the tools of dynamic modular analysis, examining seven intrinsic systems of the brain that are relied upon for a number of different cognitive functions. By representing distinct time periods of data as separate slices of a multislice network, we are able to assess the interaction of the various regions and functional systems of the brain over time.

In Chapter 4, we introduce metrics from graph theory (developed by Donnat et al. [30]) that are able to assess distances between networks representing distinct time periods. By using 'global' distance metrics we are able to examine the holistic transformations of the networks between time windows and by using 'local' metrics we are able to investigate changes at the nodal level. Finally, we investigate a number of methods that provide a balanced view between local and global methods, examining networks at the nodal, regional, and entire network level. To the best of our knowledge, these metrics have not been applied to brain MEG data in order to investigate brainwaves of different frequencies.

Chapter 5 uses the tools introduced throughout the thesis to investigate the structural and dynamical differences between male and female brains. In particular, this thesis contributes to the neuroscientific field by applying the distance metrics presented to differentiate between the different frequency brainwaves of male and female brains.

The thesis concludes in Chapter 6 with a discussion of the main results of our work and potential avenues of exploration for future research.

Chapter 2

Static modular analysis

In this chapter, we focus on analysing the structural properties of the brain from a static point of view. By preprocessing the subject MEG data into adjacency matrices, we are able to utilise tools from graph theory to assess the modular organisation of the brain. In particular, we seek to take advantage of the improved temporal resolution of MEG data to discover any structural differences between the brain at different frequencies. This static analysis, when combined with the dynamic analysis in Chapter 3, will enable us to determine if any differences we find between male and female brains are structural or dynamical[1].

2.1   Subject selection and data collection

The subject data analysed throughout this thesis has been accessed via the Human Connectome Project (HCP) Young Adult study[2], which provides open-access neural data. Specifically, this includes MEG data for 95 subjects, of which 89 were recorded during resting-state. Subjects were selected to provide an equal split of males and females from two age groups. 30 healthy subjects (15 males and 15 females) were chosen: 24 subjects aged 26–30, 12 females; 6 subjects aged 31–35, 3 females.

All participants underwent a 6 minute resting-state MEG scan acquired with a Magnes 3600 (4DNeuroimaging, San Diego, Ca) with 248 magnetometers within a shielded room with 64 EEG Voltage Channels and 23 MEG reference channels (5 gradiometers and 18 magnetometers). Five current coils attached to the subject, in combination with structural imaging data and head surface tracings, were used to

---

[1]The code used to implement all static modular analysis in this thesis was produced by the author.

[2]The data is publicly available on the HCP website [31].

localise the brain in geometric relation to the magnetometers. The same coils were used to monitor and partially correct for head movement during the MEG acquisition session (Velmurugan et al. [32]). Participants were scanned (with a sampling rate of 1000 Hz and a DC bandpass of 330 Hz) lying quietly with their eyes open and fixated on a cross on a screen in front of them with the room lights off. Participants were instructed to avoid structured thinking and to let their mind wander (i.e. resting-state condition). The position of each participant's head was monitored continuously through head position indicator coils affixed to the participant's head. Following the MEG scan, a 3T MRI (GE) high resolution T1 anatomical image was obtained for source localisation during data preprocessing.

2.2 MEG data preprocessing, regions of interest and beamforming

The MEG data was preprocessed using the same approach described in Kim et al. [33] and Kisler et al. [34]. To analyse the resting-state data we used the FieldTrip toolbox, run on MATLAB software (verR2015b). The first and last 40 seconds of the recorded data were removed, leaving 280 seconds of resting-state data for each participant. Data were band pass-filtered between 1 and 150 Hz and a notch filter was applied at 60 Hz. Down sampling to 300 Hz was then performed and independent component analysis (ICA) used ("runica" function) to remove artefacts associated with eye blinks, breathing and muscle activity. This was done by visually inspecting the different components and removing components that appeared to be noise or periodic signals. The procedure for visual ICA removal varied for each subject as some subjects had more noise than others. Thus, there was a range of components that were removed but fewer than 15 out of 204 components for each subject. To register the resting-state MEG data to the participant's anatomical image, the fiducial points of the nasion and bilateral preauricular were first identified on the anatomical image and these were used to co-register the MEG data to the anatomical image. After each person's MEG data is registered to their own MRIs by using fiducial points defined before the MEG scan, each individual's preprocessed data is then warped into a template brain. The anatomical image was then segmented using statistical parametric mapping (SPM), resulting in a geometrical representation of the brain which was then used in a single-shell forward model.

A linearly constrained minimum variance beamformer (see Veen et al. [35] and Hillebrand et al. [36]) was used to extract a continuous time series for nodes of the

automated anatomical labelling (AAL) atlas (Long et al. [37]). Thus, 98 nodes, or regions of interest (ROIs), were defined and used as "virtual sensors". These node coordinates (x, y, z), in the Montreal Neurological Institute and Hospital (MNI) coordinate space, are available in Appendix A, and their corresponding position in the brain can be seen in Figure 2.1.
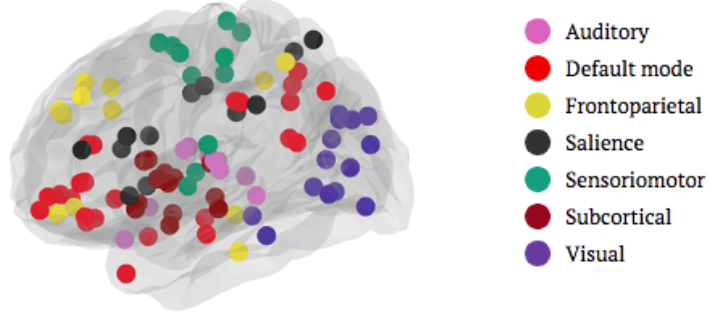
Figure 2.1: 98 regions of interest (ROIs) of the brain and their functional system affiliation, as found in the AAL atlas.

From the extracted time-series of each node, the functional connectivity (FC or coupling) values were calculated across each pair of nodes using the mathematical formula for amplitude envelope correlation (Liu et al. [38]).

For each time point in the resting-state time-series, the instantaneous phase and amplitude was calculated with the Hilbert Transform. For the Hilbert Transform, a finite impulse response filter was used to divide the time-series data into frequency bands: delta (1–4 Hz), theta (4–8 Hz), alpha (8–13 Hz), beta (13–30 Hz), low gamma (30–60 Hz), and high gamma (60–150 Hz). In order to remove linear dependencies from the signal and to control for source leakage, orthogonalisation was applied to the time-series in each ROI (node) using the ROI-nets toolbox (Colclough et al. [39]). Orthogonalisation takes a set of non-orthogonal independent functions and creates an orthogonal relationship between them. In amplitude envelope correlation this process removes false coupling between two different sources which may have signals originating from the same source. Each participant's resting-state scan was divided into epochs of 10 seconds, resulting in 28 epochs of data that are considered as 28 successive time frames in our work.

Here, we determined a static and dynamic functional coupling for each frequency band in each participant by creating a functional connectivity matrix. Firstly, we created a 98×98 individual functional connectivity matrix to represent the static state as the epoch average over the 28 epochs for each of the 6 frequency bands. Secondly, to determine the dynamic fluctuation of the interaction strength between

brain regions, 168 functional connectivity matrices were formed for each subject, 1 matrix for each of the 28 time windows and for each of the 6 frequency bands.

As well as indicating the mapping of the ROIs to the brain, Figure 2.1 shows which of the seven functional systems each ROI is affiliated to (see Appendix A for the full list of ROIs and their system affiliation).

2.3 Thresholding function

Once the MEG data has been preprocessed, the resulting 98×98 functional connectivity matrices are dense, with pairwise positive or negative correlations between all of the 98 ROIs of the brain. One of our goals is to use distance metrics to investigate brain networks. However, the axioms of a distance metric require non-negative values [40, p. 229], meaning we have to amend our matrices before applying the metrics. Additionally, some of the graph theory tools used in this thesis are only effective on sparse matrices. For example, if we generated graphs from the dense functional connectivity matrices as they are, it would theoretically be expected that these graphs would have low modularity, equivalent to a random graph [26]. We therefore aim to remove negative correlations from the functional connectivity matrices, before converting them to sparse matrices.

The approach for removing negative correlation values from functional connectivity matrices is currently divided. One option is to consider the sign of the correlation coefficients by analysing the community structure in complex networks with weighted and signed links[3]. Alternatively, another option is to consider the absolute values of all correlations[4].

In this thesis, one of our aims is to investigate the relevance of applying new dynamic graph analysis and distance metrics to MEG data. Therefore, we have chosen to only focus our analysis on positive correlations in order to simplify the approach. Consequently, we set the negative correlations to 0, deciding to only assess pairwise correlations that display non-negative values. By removing negative correlations from the matrices, the mean density of all the functional connectivity matrices across subjects decreases from 1.00 to 0.77 (i.e. 77% of the elements of the resulting functional connectivity matrices are non-zero).

Once the negative correlations have been removed, the resulting matrices still remain too dense for our analysis. We therefore want to apply a thresholding

---

[3]See Traag and Bruggeman [41], for example, for further discussion.
[4]See Achard et al. [42], for example, for further discussion.

function that can convert the dense functional connectivity matrices to sparse matrices. There are a number of different methods for forming sparse representations of dense functional connectivity matrices proposed in the literature. We proceed by introducing an approach proposed by Slater et al. [43], which is primarily used for analysis throughout this thesis.

Slater et al. [43] introduced a two-stage algorithm for extracting the multiscale backbone of complex weighted networks. Given an $N \times N$ matrix, the first stage of the algorithm begins by scaling the sum of the first row, and then first column, to equal 1. This is then repeated for rows and columns $2, 3, \ldots, N-1$, before iteratively repeating this row and column scaling until the matrix sufficiently converges to a doubly stochastic table (i.e. all row and column sums converge to 1).

The second stage of the algorithm proceeds by forming an $N \times N$ adjacency matrix, where the elements corresponding to the largest elements in the doubly stochastic table are added one at a time. This is continued until the adjacency matrix represents a graph that is formed as a single strong component. This creates a binary network where all edges are assigned a value of 1. By using this approach, the graphs are always connected in the sense that there exists a path between every pair of nodes. After applying this thresholding algorithm to the data for each of the subjects, the mean density of the matrices across subjects is reduced from 0.77 to 0.09. We make a note that although the mean density has decreased to 0.09, this is variable across all the matrices.

In order to investigate the effect that this edge density has on the results presented in this thesis, we repeat all analysis with adjacency matrices formed using an alternative thresholding method as introduced by Meunier et al. [26]. This thresholding method creates adjacency matrices with consistent edge densities (see Appendix B for full explanation of method).

2.4   Community detection

Community detection, which involves partitioning a network into natural clusters that provide insight into the structure of the network [44], is of interest in a wide variety of fields across the natural, social and information sciences. In the context of neuroscience, the goal is to investigate the topological structure of the human brain in order to examine natural partitions of the brain's functional networks into a set of communities, or modules. The goal is to form communities such that densely intraconnected nodes are sparsely interconnected with nodes in other communities.

There have been several proposed methods for detecting communities in a network[5]. Two of the most commonly used approaches include the stability method, as introduced by Delvenne et al. [44], and the Louvain algorithm, as introduced by Blondel et al. [46]. The methods approach the problem of detecting communities from different angles. On the one hand, the stability method aims to maximise the likelihood of a random walker remaining within the community it begins in over a specified period of time. On the other hand, the Louvain algorithm optimises the modularity of a given network. More recently, Traag et al. introduced the Leiden algorithm [47], which guarantees communities are well-connected. The Leiden algorithm addresses an issue with the Louvain algorithm, where the communities produced are sometimes not internally connected.

In this thesis, we use the Louvain algorithm, which is widely regarded as one of the best algorithms for detecting communities and has been the method of choice in numerous brain studies [13, 14, 48, 49, 50]. To understand the algorithm, we first need to understand the underlying principles of modularity.

Consider a network with N nodes. The idea of modularity is to compare the number of links connecting the N nodes to the expected number of links in an appropriate null model. Methods aimed at identifying superior modularity are designed by choosing a value function and then finding the partition that maximises this function. We proceed by maximising one of the most commonly used value functions, introduced by Newman and Girvan [51]. For a given network, the function measures the proportion of a network's edges that fall within communities minus the proportion of edges that would be expected in an equivalent random model.

Consider a graph G formed of N nodes and M edges. The associated adjacency matrix A is defined by

$$A_{ij} = \begin{cases} 1 & \text{if } i \text{ and } j \text{ are adjacent} \\ 0 & \text{otherwise.} \end{cases}$$

The Newman-Girvan modularity value function is then defined by

$$Q = \frac{1}{2M} \sum_{c=1}^{N_{CM}} \left[\sum_{\substack{i,j=1; \\ v_i, v_j \in CM_c}} (A_{ij} - B_{ij}) \right], \tag{2.1}$$

where the cth community $(c = 1, 2, \ldots, N_{CM})$ is denoted by CM_c. Denoting the degree of node i by k_i, we set $B_{ij} = k_i k_j / 2M$ as the probability that nodes v_i

---

[5]See El-Moussaoui et al. [45] for a comprehensive review of the types of methods available.

and v_j are adjacent, given a random graph comparable to graph G (as in the configuration null model [52]). Denoting the number of links connecting two nodes within community CM_c by M_c, Q can be rewritten as

$$Q = \sum_{c=1}^{N_{CM}} \left[\frac{M_c}{M} - \left(\frac{\sum_{i=1; v_i \in CM_c}^{N} k_i}{2M} \right)^2 \right]$$

$$= \frac{1}{2M} \sum_{i,j=1}^{N} \left(A_{ij} - \frac{k_i k_j}{2M} \right) \delta(g_i, g_j), \tag{2.2}$$

where

$$\delta(g_i, g_j) \quad = \quad \begin{cases} 1 & g_i = g_j \\ 0 & \text{otherwise,} \end{cases}$$

and g_i is the community that the ith node belongs to.

The Kronecker delta function, δ, ensures that only intramodular edges are added to the sum. Newman and Girvan suggested that modularity values of $Q \geq 0.3$ are indicative of non-random community structure [51].

The goal of the Louvain algorithm is to maximise (2.2). The algorithm works by repeatedly performing two phases. The first phase begins by assigning a distinct community to each node of a network. Working through the nodes, one at a time, the algorithm assesses whether joining each node with any of its neighbours increases the networks modularity. If so, the node is joined to the neighbouring node which increases the modularity the mode; otherwise, the node stays in its original community. This is repeated iteratively until the modularity of the network is no longer improved. The second phase forms a new network, with one vertex representing each community from the results of the first phase. The edge weight in between each pair of communities is the sum of the weights of the edges linking the two communities. Once this second phase is complete, the algorithm loops back to the first phase and repeats the analysis. This continues iteratively until the modularity of the network is no longer increased on the next iteration of the algorithm and thus the maximum modularity has been attained[6]. By determining the modularity of our networks, the Louvain algorithm enables us to compare the quality of their partitions.

---

[6]See Blondel et al. [46] for further discussion.

2.5 Community assessment

Another method to compare the community structure of networks is the normalised mutual information (NMI) approach. The normalised mutual information approach, outlined in Alexander-Bloch et al. [17], aims to examine the difference in community structure between two groups. By treating two modular partitions as random variables, X and Y, Kuncheva and Hadjitodorov [53] described their mutual information as

$$MI(X,Y) = \sum_{x,y} P_{XY}(x,y) \log \left(\frac{P_{XY}(x,y)}{P_X(x)P_Y(y)} \right), \tag{2.3}$$

where $P_X(x)$ is the probability of distribution x and $P_{XY}(x,y)$ is the joint probability distribution of x and y.

This information can be used to create a measure of similarity between two partitions. Given two networks with partitions G and $\bar{G}$, let C_G and $C_{\bar{G}}$ be the number of modules in each partition. Let N be the number of nodes in the networks; N_{ij} the number of common nodes between module i of G and module j of $\bar{G}$; and N_i and N_j the number of nodes in module i of G and module j of $\bar{G}$ respectively. The similarity between two community structures, G and $\bar{G}$, can then be quantified by their normalised mutual information

$$NMI(G, \bar{G}) = \frac{-2 \sum_{i=1}^{C_G} \sum_{j=1}^{C_{\bar{G}}} N_{ij} \log \left(\frac{N_{ij}N}{N_i N_j} \right)}{\sum_{i=1}^{C_G} N_i \log(\frac{N_i}{N}) + \sum_{j=1}^{C_{\bar{G}}} N_j \log \left(\frac{N_j}{N} \right)}, \tag{2.4}$$

where the convention $0 \times \log(0) = 0$ is used. Note that the NMI of two partitions always lies between 0 and 1; the NMI of two independent graphs is 0 and the NMI of two identical graphs is 1.

In order to analyse the structure of the brain networks from a static perspective, we proceed by finding the mean of the functional connectivity matrices across the 28 time windows, resulting in one matrix for each frequency band. The thresholding function from Section 2.3 is then applied to transform these matrices into adjacency matrices, before the Louvain algorithm determines a natural partition for each one. Once the modularity of the final partitions has been determined by optimising (2.2), we calculate the mean modularity across all subjects for each band.

Table 2.1 shows the results of this analysis. The table highlights that the networks of the delta, theta, alpha, and beta bands show similar levels of modularity. However, there was a statistically significant difference between the modularity of frequency bands as determined by one-way ANOVA ($F(5, 174) = 62.08$; $p < 0.0001$), which the

table suggests may be the low and high gamma bands. To confirm this, we perform multiple pairwise comparisons using a Tukey HSD test. The results highlight that the mean modularity for the low gamma (mean = 0.660; standard deviation = 0.037) and high gamma (mean = 0.623; standard deviation = 0.049) were significantly different to the other bands (p-tukey = 0.001 for all pairwise comparisons; see full breakdown of results in Table D.1 in Appendix D).

Frequency band	Mean modularity	Mean pairwise NMI
Delta	0.714	0.684
Theta	0.727	0.687
Alpha	0.729	0.703
Beta	0.731	0.702
Low gamma	0.660	0.661
High gamma	0.623	0.605

Table 2.1: Mean modularity of the partitions of the networks of all subjects for each frequency band, and pairwise normalised mutual information between all networks within each band.

Similarly, we are able to determine the mean pairwise NMI between all 30 subjects *within* each frequency band, which is also displayed in Table 2.1. In order to run a one-way ANOVA test, we use the 435 pairwise NMI values between the 30 subjects as the data set for each frequency band (notice that $NMI(A, B) = NMI(B, A)$ and $NMI(A, A) = 0$). We once again find a statistically significant difference between the mean NMI of the bands ($F(5, 2604) = 145.9$; $p < 0.0001$). As before, we proceed by performing multiple pairwise comparisons using a Tukey HSD test. Once again, the mean NMI values for the low gamma (mean = 0.661; standard deviation = 0.066) and high gamma (mean = 0.605; standard deviation = 0.078) were significantly different to the other bands (p-tukey = 0.001 for all pairwise comparisons; see full breakdown of results in Table D.2 in Appendix D). These results suggest that networks of the higher frequency bands may display different structural properties to the lower frequency bands.

To understand more about the interactions between frequency bands, we now calculate the mean pairwise NMI for the 30 subject networks *between* each pair of bands. The results of this are presented in Figure 2.2. We see that the NMI values between the networks of the higher frequency bands (low and high gamma) and all other bands are relatively low, with high gamma being the lowest. NMI values between the delta, theta, alpha and beta networks are all consistently high.

15

These results suggest that the lower frequency bands are relatively similar to each other when viewed statically. As the frequency increases, the networks become more dissimilar, with high gamma networks being the most distinctive.
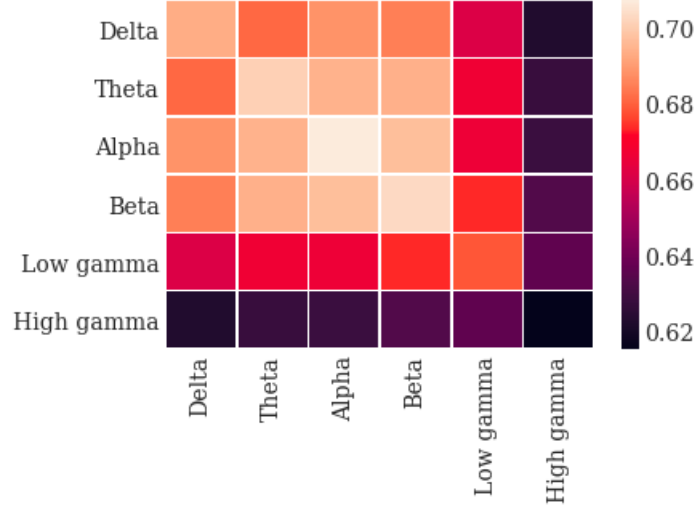
Figure 2.2: The mean NMI of all pairs of networks between frequency bands.

These results suggest that the low and high frequency bands show different brain architecture (i.e. they are structurally different). This makes sense since brain processes occurring in lower frequency bands are based on a different brain structure to the cognitive functions in higher frequency bands (see Table 2.2 for examples of brain states that characterise each frequency band).

Frequency band	Frequency (Hz)	Brain states
Delta	1–4	Sleep
Theta	4–8	Deeply relaxed
Alpha	8–13	Passive attention
Beta	13–30	Busy, active mind
Low gamma	30–60	Concentration
High gamma	60–150	Problem solving

Table 2.2: Characteristics of MEG brain waves of six different frequencies. Table adapted from [54].

Chapter 3

Dynamic modular analysis

The intrinsic modular architecture of the human brain cannot solely be viewed from a static point of view due to temporal fluctuations in functional connectivity patterns. Therefore, this chapter applies dynamic modular analysis techniques, developed by Finc et al. [13] and Bassett et al. [55][7], to brain networks in order to reveal how the brain's structural properties behave over time. By summarising community assignment of ROIs in the brain over the time windows in a *modular allegiance matrix*, we aim to investigate how ROIs in each of the seven cortical systems interact while subjects are in resting-state. Examining the interaction at both node and system level provides insight into the different levels of detail that are driving changes in the brain networks.

It is common practice to represent temporal networks by multislice networks, where consecutive slices represent consecutive time periods. It is once again natural to seek communities within our networks to represent the brain's structure across the time windows. In order to do this, we use a generalised Louvain-like community detection algorithm as introduced by Mucha et al. [58] to determine communities across the multislice networks.

3.1 Generalised Louvain algorithm

In this chapter, the networks for each of the 28 time windows are considered as consecutive slices of a multislice network. For a given slice s, A_{ijs} denotes the adjacency between node i and j in slice s. We also denote the interslice strength of node j in slice s by $k_{js} = \sum_i A_{ijs}$ and across slices by $c_{js} = \sum_r C_{jsr}$. The strength

---

[7]The code for these methods, used as a basis to implement the dynamic modular analysis in this thesis, is publicly available here: Finc et al. [56]; Bassett et al. [57].

and community assignment of node j in slice s are denoted by $\kappa_{js} = k_{js} + c_{js}$ and g_{js} respectively. In their paper, Mucha et al. [58] develop a multislice generalisation of modularity

$$Q_{\text{Multislice}} = \frac{1}{2\mu} \sum_{ijsr} \left\{ (A_{ijs} - \gamma_s V_{ijs}) \, \delta_{sr} + \delta_{ij} C_{jsr} \right\} \delta(g_{is}, g_{jr}), \qquad (3.1)$$

where μ is the total edge weight of the network, δ_{ij} is the Kronecker delta, and γ_s is the resolution of slice s, a free parameter. For our analysis, we set $\gamma = 1$, in line with previous dynamic brain analysis studies [13, 14]. Using the Newman-Girvan null model

$$V_{ijs} = \frac{k_{is} k_{js}}{2m_s}, \qquad (3.2)$$

where $m_s = \frac{1}{2} \sum_{ij} A_{ijs}$ is the total edge weight of slice s, the modularity quality function becomes

$$Q_{\text{Multislice}} = \frac{1}{2\mu} \sum_{ijsr} \left\{ \left(A_{ijs} - \gamma_s \frac{k_{is} k_{js}}{2m_s} \right) \delta_{sr} + \delta_{ij} C_{jsr} \right\} \delta(g_{is}, g_{jr}). \qquad (3.3)$$

We consider this for the six frequency bands for each subject, and perform 100 optimisations of the modularity quality function[8]. After running the community detection algorithm, we produce 100 $N \times T$ module assignment matrices, where N is the number of nodes of each network and T is the number of slices (or time windows). Each matrix element (i, j) represents the community of node i in slice j. From the results of running the generalised Louvain algorithm, we are able to define a number of metrics which can help describe the community dynamics of the networks.

3.2   Flexibility

One metric that we are able to define at node, system, and network level to investigate community dynamics of a multislice network is *flexibility*. Beginning at node (ROI) level, the flexibility of a node is informally defined as the number of times that a node changes community across slices, normalised by the total number of possible times it could have changed communities. More formally, Papadopoulos et al. [60] defines the flexibility of node i by

$$\xi_i = \frac{h_i}{T - 1}, \qquad (3.4)$$

---

[8]The code to run the generalised Louvain algorithm was developed by Jeub et al. [59].

where h_i is the number of times that node i changes communities across slices, and T is the number of slices.

As we mentioned earlier, we also want to be able to examine regional changes between networks. For this, we identified seven functional systems of the brain in Section 2.1. In order to determine flexibility of a given system, we simply find the mean flexibility of all nodes in that system. Formally, this is defined as

$$\xi_S = \frac{1}{n_S} \sum_{i \in S} \xi_i, \tag{3.5}$$

where n_S is the number of nodes in system S.

Finally, we also want to be able to perform analysis at the entire network level. Therefore, as in Papadopoulos et al. [60], we define the flexibility of the multislice network as a whole by the mean flexibility of all nodes

$$\Xi = \frac{1}{N} \sum_{i} \xi_i, \tag{3.6}$$

where N is the number of nodes. At all three levels, the flexibility can be viewed as a measure of rearrangement, with a higher flexibility value meaning that the nodes have changed communities frequently. In terms of our brain networks, flexibility offers us a metric to understand more about how the brain evolves over time. For example, a system with high flexibility suggests that the system may be interacting with many different regions of the brain. To investigate this further, we need to define complementary metrics that provide more information about the dynamics of the brain's communities.

3.3 Promiscuity

Another metric we are able to define at node, system, and network level is *promiscuity*. The promiscuity of a node within a multislice network corresponds to the fraction of the total number of communities of which a node is a member one or more times. Whereas flexibility sheds light on how much the community structure evolves over the slices, the promiscuity provides insight into how much the node is spread across different communities over the time windows. For example, if a node has high flexibility, we know that it is changing communities a lot. However, promiscuity allows us to determine whether a node changes repeatedly between two communities (and thus has a low promiscuity value), or whether it is changing between many communities (and thus has a high promiscuity value).

As defined in Sizemore and Bassett [55], the promiscuity of node i is defined by the number of communities that i is a member of, divided by the total number of communities of the network. We note that the promiscuity of a node is 0 if it is a member of the same community throughout all slices, and 1 if it is a member of all communities of the network.

In a similar way to flexibility, the promiscuity of system S is defined as

$$\phi_S = \frac{1}{n_S} \sum_{i \in S} \phi_i, \tag{3.7}$$

and the promiscuity of the entire network as

$$\Phi = \frac{1}{N} \sum_i \phi_i. \tag{3.8}$$

We proceed by calculating the mean flexibility and promiscuity across the 30 subjects for each of the seven functional systems. The results, displayed for all six frequency bands in Figure 3.1, highlight a strong similarity between the flexibility and the promiscuity of the 98 ROIs.

(a) Flexibility
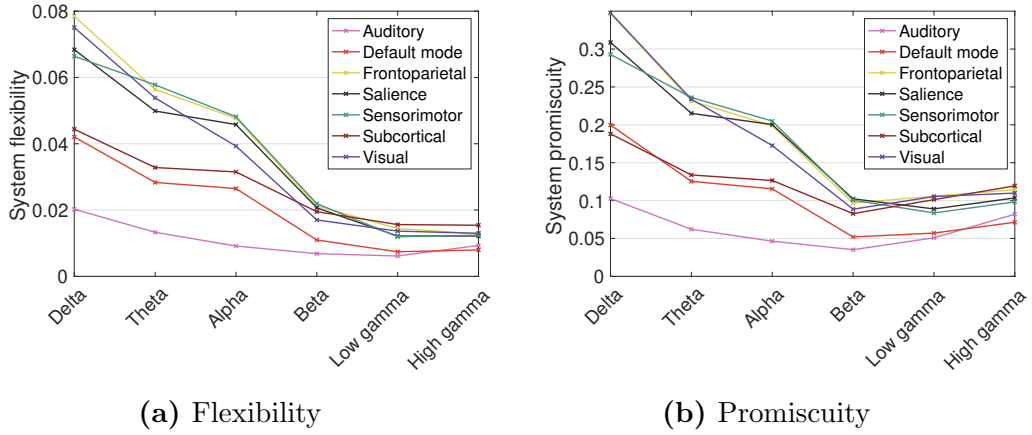
(b) Promiscuity

Figure 3.1: Mean functional system level flexibility and promiscuity across all subjects for each frequency band. Calculated as the mean of the nodes within each system.

Additionally, there is a strong correlation between the frequency of the bands and both the system flexibility and promiscuity. In general, the higher frequency bands displayed lower flexibility and promiscuity; however, the values seem to flatten out or even increase at the low and high gamma frequency bands. This suggests we are seeing different levels of rearrangement across the frequency bands, with greater rearrangement for the bands of lower frequency. Finally, we notice the difference in

the flexibility and promiscuity values of each system. The auditory system has a low level of both flexibility and promiscuity across the frequency compared to the other systems, particularly for the lower frequency bands. This means, relative to the other systems, the nodes within the auditory system are remaining in the same communities throughout time windows.

3.4   Modular allegiance matrix

Representing the brain as a network, several papers have studied the dynamics of the brain through community assignment analysis of the network's nodes across multislice networks [13, 14, 27]. Realising that the modular architecture of functional brain networks fluctuates over time, these papers aim to measure this change. One of the proposed methods for measuring this change is the modular allegiance matrix, P. Each matrix element P_{ij} represents the proportion of slices in which node i and node j are assigned to the same community.

Denote the number of optimisations of the generalised Louvain algorithm by O and number of time windows by T. As found in Mattar et al. [14], the modular allegiance matrix is then formally defined by

$$P_{ij} = \frac{1}{OT} \sum_{o=1}^{O} \sum_{t=1}^{T} a_{i,j}^{k,o}, \qquad (3.9)$$

where, for each optimisation o and time window t,

$$a_{i,j}^{k,o} = \begin{cases} 1 & \text{if nodes } i \text{ and } j \text{ are in the same module} \\ 0 & \text{otherwise.} \end{cases}$$

For our analysis, we use $O = 100$ and $T = 28$.

In Figure 3.2, the modular allegiance matrix for the mean across subjects and frequency bands has been calculated. This has been done by computing the modular allegiance matrix for each of the six frequency bands and 30 subjects separately, and then taking the mean value for each element of the 180 matrices. The darker red cells along the diagonals of the matrix highlight the fact that ROIs from the same system tend to belong to the same community throughout time windows; this particularly seems to be the case for the visual system (purple). The darker blue cells, for instance found along the bottom and the right-hand side of the matrix, suggest that these systems tend to belong to different communities throughout time windows. This suggests that nodes in the visual system tend to be found less frequently in communities with nodes from other functional systems.

21
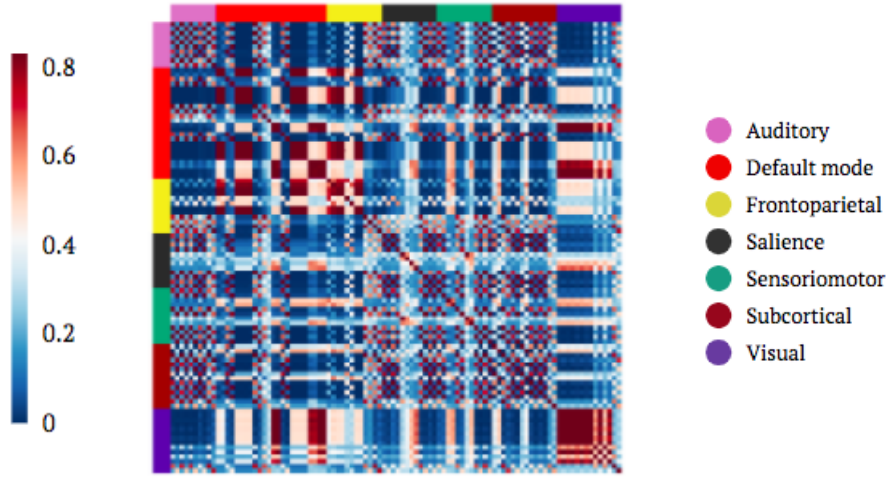
Figure 3.2: Modular allegiance matrix at ROI level. Element (i, j) is the probability that nodes i and j belong to the same community within a single layer of the multilayer network. ROIs are grouped into their functional systems, represented by the colour bands along the axes of the matrix.

3.5   Recruitment and integration

3.5.1   Nodal level

In order to further investigate the structural properties of the networks over time, new metrics can be calculated from the elements of the modular allegiance matrix. Noting the system affiliation introduced in Section 2.1, the dynamic network *recruitment* coefficient for a given node i with respect to a system S is defined by

$$R_i^S = \frac{1}{n_S} \sum_{j \in S} P_{ij}, \tag{3.10}$$

where n_S is the number of nodes in system S. Informally, R_i^S represents the average probability that the ith node is in the same community as other nodes in system S. If a node has a high recruitment coefficient with respect to a certain system, that means it is found in that system across many time windows.

We proceed by calculating the mean recruitment across all subjects for each of the 98 ROIs, for each frequency band. The 98 values have then been divided so that the lighter ROIs have a lower recruitment and the darker ROIs have a higher recruitment. This has been done by subtracting the lowest value of recruitment from the highest value, and then dividing the result into 6 equal divisions, before prescribing a colour to each ROI depending on which division it fell in. The results, displayed in Figure 3.3, highlight the higher recruitment values for the higher frequency bands, low and

high gamma. Similarly, we see by inspection that the visual system, whose nodes are found at the right-hand side of the images, tends to have a higher level of recruitment for all frequency bands. This implies that the nodes of the visual system tend to remain in the same communities as other ROIs from the visual system. This analysis suggests it is worth exploring the modular allegiance metrics at functional system level, which we do in Section 3.5.2.

(a) Delta   **(b)** Theta   **(c)** Alpha

(d) Beta   **(e)** Low gamma   **(f)** High gamma

Low   High
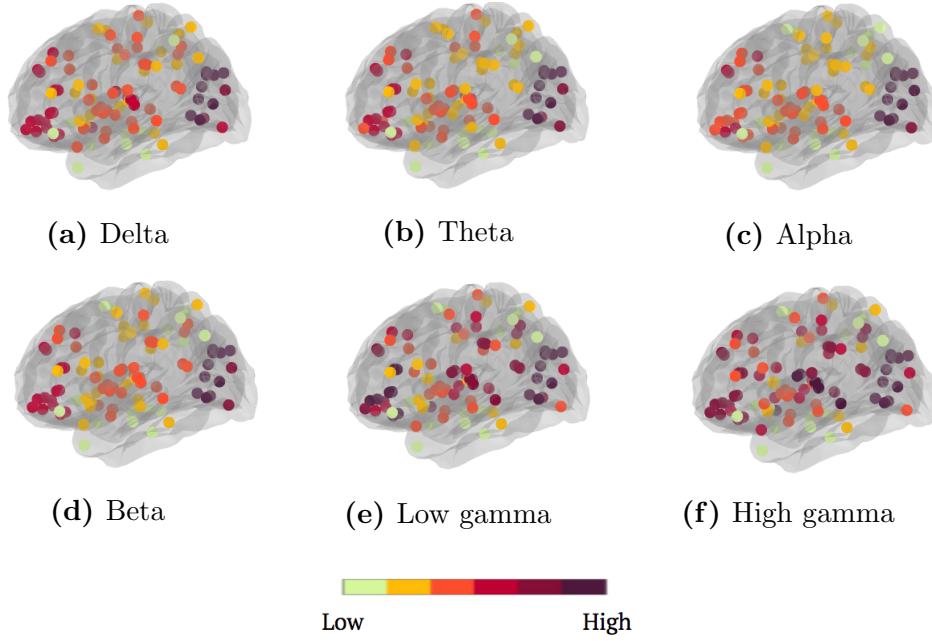
Figure 3.3: Mean recruitment coefficients of each ROI across all subjects, displayed for each frequency band. The darker the circle of the ROI, the higher the recruitment, representing an increased probability that the ROI is found in the same community as other ROIs from its own system.

Similarly, the dynamic network *integration* coefficient for a given node i with respect to a system S is defined by

$$I_i^S = \frac{1}{N - n_S} \sum_{j \notin S} P_{ij}, \tag{3.11}$$

where N is the total number of nodes of the network. Informally, I_i^S represents the average probability that the ith node is in the same community as nodes from systems *other* than system S. If a node has a high integration coefficient with respect to a system S, that means it tends to be found in systems other than system S across the time windows.

23

3.5.2   System level

In order to examine the dynamics of the brain at a higher level, we now introduce recruitment and integration coefficients at the system level. The goal is to gain a deeper understanding of how systems interact over the time period. The recruitment coefficient of a given system S is defined by

$$R_S = \frac{1}{n_S^2} \sum_{i \in S} \sum_{j \in S} P_{ij}. \tag{3.12}$$

If a system has a high recruitment coefficient, this means that the ROIs of the system tend to be part of the same community throughout time windows.

Similarly, the integration coefficient between two systems, S_1 and S_2, is defined by

$$I_{S_1 S_2} = \frac{1}{n_{S_1} n_{S_2}} \sum_{i \in S_1} \sum_{j \in S_2} P_{ij}, \tag{3.13}$$

where n_{S_1} and n_{S_2} are the number of nodes in system S_1 and S_2 respectively. If two systems have a high integration coefficient, then the nodes of those two systems tend to be part of the same community throughout time windows.

The recruitment coefficients of the seven functional systems of the brain and their pairwise integration coefficients can be viewed in Figure 3.4 for the mean across all subjects and frequency bands. The size of the node represents the recruitment of that system, and the edge thickness represents the integration between the two connected systems. This figure highlights the high recruitment of the visual system, as well as the low integration of the visual system with respect to the other systems. In particular, the integration of the visual system and the auditory system is significantly below the mean ($p < 0.05$).

In Figure 3.5, we show the system level modular allegiance matrices for the mean of all 30 subjects for each frequency band. The diagonal element of the matrix for each subject represents the recruitment of system i, and element (i, j) represents the integration between system i and system j. It is clear to see that the frequency band seems to have a more general effect on the modular allegiance coefficients, with the low and high gamma bands having much higher values of recruitment and integration. In order to understand the role of the systems at a higher level, we calculate the mean across all six frequency bands. First, however, we normalise the system level recruitment and integration coefficients based on the number of nodes in each system to remove potential bias.
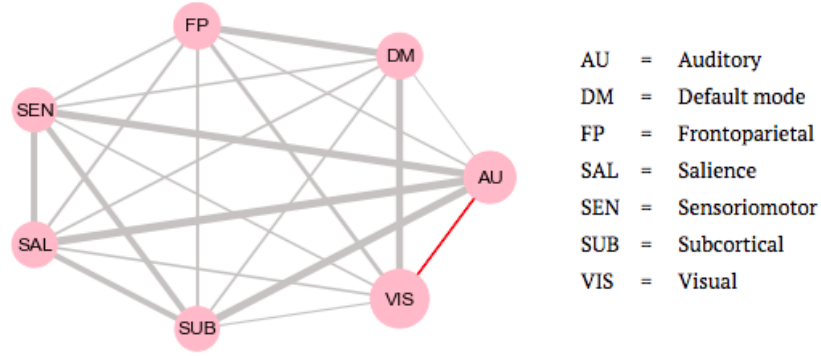
Figure 3.4: Graph representing the recruitment and integration coefficients of the functional systems, where the coefficients are the mean across subjects and frequency bands. The size of the node represents the recruitment of the system, and the edge thickness represents the integration between two systems. The red edge highlights that the integration between the AU and VIS systems is significantly below the mean ($p < 0.05$).
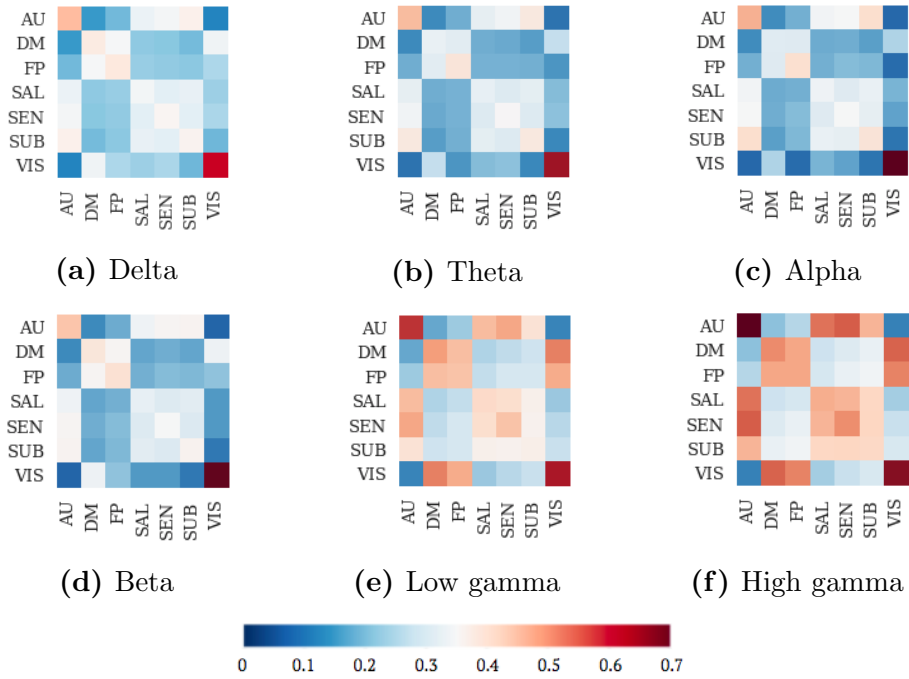
Figure 3.5: System level modular allegiance matrices, where each element represents the mean of the corresponding elements in the system modular allegiance matrices for the 30 subjects. Functional system abbreviations: auditory (AU), default mode (DM), frontoparietal (FP), salience (SAL), sensorimotor (SEN), subcortical (SUB), visual (VIS).

3.5.3 Normalisation of system level recruitment and integration

To normalise the coefficients, a permutation approach is used, where we form 1000 null modular allegiance matrices from graphs that have been created randomly using the actual number of nodes for each functional system. This provides us with null distributions of the recruitment and integration coefficients based on the size of the systems. After running this 1000 times, we divide the recruitment and integration coefficients of the actual data by the coefficients of the null model in order to determine the normalised coefficients. We proceed by forming a mean system modular allegiance matrix across the subjects, and then normalising the coefficients. Both the original and the normalised matrices are shown in Figure 3.6.

(a) System modular allegiance matrix

(b) Normalised system modular allegiance matrix
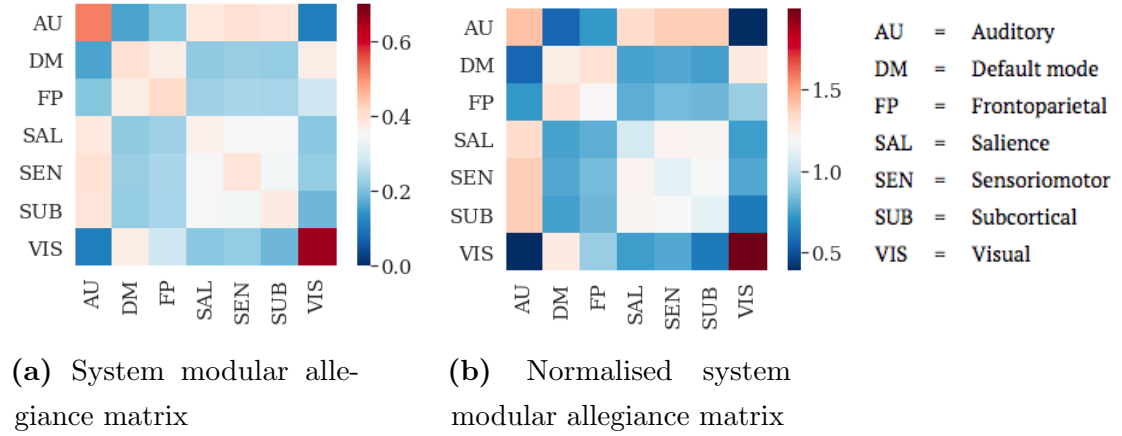
Figure 3.6: **(a)** System level modular allegiance matrices, where each element represents the mean of the corresponding elements in the system modular allegiance matrices for all subjects and frequency bands. **(b)** A normalised version of the system modular allegiance matrix, where the coefficients have been normalised to remove potential bias produced by the different number of nodes in each system.

We are able to see that the default mode, frontoparietal, and visual systems seem to have relatively low integration coefficients with respect to the other systems. We also note that the recruitment of the visual system and the integration of the auditory and visual systems are assessed to be outliers of both of the system modular allegiance matrices[9]. It is clear that nodes of the visual and audio systems are quite stable and stay in their respective system across time windows, as implied by their high recruitment. However, their low integration means that the ROIs of these two

---

[9]The coefficients are assessed to be outliers if they are found to be outside of the range of the mean of the matrix elements plus or minus two standard deviations.

systems do not tend to be part of the same community throughout time windows. This suggests that nodes within the auditory and visual system do not interact a great deal across time windows.

The dynamic methods introduced in this chapter have contributed to the previous static analysis by examining the structural properties of the brain across the time windows. By inspecting the community assignment of our networks, we have also been able to explore the differences in modular organisation of the intrinsic functional systems of the brain for each of the frequency bands. In order to offer a new perspective on the dynamics of the brain, the next chapter introduces several distance metrics capable of determining the level of transformation of the brain between time windows.

Chapter 4

Distance metrics

Calculating distances between networks that represent different time windows enables us to examine the structural changes of the human brain over time, and whether this change is dependent on the frequency of the MEG data. In this chapter, we introduce distance metrics presented by Donnat et al. [30], who used the metrics to assess fMRI data of cocaine-dependent patients, highlighting a correlation between cocaine-dependency and differences between brain connectomes. We note, however, that research on applying distance metrics to MEG data is scarce and thus we aim to shed new light on dynamic brain properties by taking advantage of the improved temporal resolution of MEG imaging.

We introduce distance metrics with different levels of granularity, beginning with two global approaches that provide a holistic view of the changes between networks. We then examine two local approaches, which provide a granular evaluation of the network changes by looking at nodal level. Finally, we introduce two mesoscale approaches that analyse graphs at the regional or neighbourhood level.

We begin by using the adjacency matrices calculated using the thresholding function introduced in Section 2.3. In Figure 4.1, the edge density of the resulting adjacency matrices are displayed (i.e. the number of edges in the network divided by the total possible number of edges). It is clear to see that the frequency bands have different edge densities once the thresholding function has been applied, with delta having the highest edge density and beta having the lowest. We keep this in mind as we perform the analysis throughout this chapter, noting that we repeat the analysis using a different thresholding function in Section 4.5. This alternative thresholding function maintains the same edge density for all networks, allowing us to see the effect of the edge densities on the results presented.
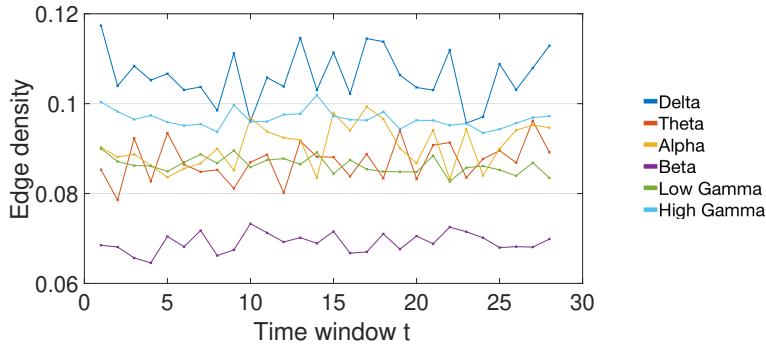
Figure 4.1: Mean edge density, across all subjects, for adjacency matrix representing time window t ($t = 1, 2, \ldots, 28$). Mean over 28 time windows (as a % of total possible edges): delta 10.6%; theta 8.7%; alpha 9.1%; beta 6.9%; low gamma 8.6%; high gamma 9.7%.

4.1 General analysis framework

For all of the distance metrics presented in this chapter, we proceed by calculating the pairwise distances between the graphs of the 28 time windows for each subject. These pairwise distances are stored in the form of a 28×28 matrix. Naturally, the diagonal elements are all equal to 0 and each matrix is symmetric to satisfy the axioms of a metric [40, p. 229].

After calculating these matrices, the goal is to visualise different aspects of the data to try to discover interesting properties of the networks. In order to do this, a new matrix is created for each frequency band, the *mean across subjects matrix*, where element (i, j) is the mean of element (i, j) of all 30 subject matrices. This can then be plotted as a *heatmap*, for example, which can be used to search for clusters of networks by seeing whether a group of networks have short distances between each other.

Additionally, the elements of each matrix can be examined to gain deeper insight into the dynamics of the networks. By inspecting the subdiagonal elements (or equivalently the superdiagonal elements), we are able to plot how the distance changes between time window t and time window $t + 1$ ($t = 1, 2, \ldots, 27$). Similarly, by examining the first row (or equivalently the first column) of the matrix, we are able to track how the distance changes between time window 1 and time window t ($t = 2, 3, \ldots, 28$). By plotting these matrix elements we can see how the distance between networks changes as the length of time between time windows increases. These visual techniques are used throughout this chapter to illustrate how different

29

methods are able to reveal a variety of interesting features of the network dynamics[10].

4.2 Global approaches

Global approaches, also known as spectral approaches, examine networks from a holistic viewpoint. In the context of brain connectome data, the global approaches provide a view of the interactions between different regions of the brain. The metrics are calculated by analysing the eigenvalues of the adjacency, Laplacian, or normalised Laplacian matrix (as defined in [61], for example). Denoting the degree of node i by k_i, as before, the degree matrix is defined by $D = \text{diag}(k_1, \ldots, k_n)$. Subsequently, the Laplacian of the adjacency matrix is defined by

$$L = D - A, \tag{4.1}$$

and the normalised Laplacian by

$$\begin{aligned} \tilde{L} &= D^{-1/2} L D^{-1/2} \\ &= I - D^{-1/2} A D^{-1/2}. \end{aligned} \tag{4.2}$$

These matrices can then be used to develop the global distance approaches presented in this section.

4.2.1 Ipsen-Mikhailov

The Ipsen-Mikhailov distance, as introduced by Ipsen and Mikhailov [62], computes a spectral distance between two graphs by comparing their spectral densities. This comparison of spectral densities aims to assess the transformation in the overall graph structure between two graphs.

Consider a hypothetical molecule formed of N particles connected by elastic strings. The adjacency matrix is defined by

$$A_{ij} = \begin{cases} 1 & \text{if there is a string between particle } i \text{ and } j \\ 0 & \text{otherwise,} \end{cases}$$

noting that $A_{ij} = 0$ for all $i = j$. We can thus describe this mechanical system by a set of N differential equations

$$\ddot{x}_i + \sum_{j=1}^{N} A_{ij}(x_i - x_j) = 0. \tag{4.3}$$

---

[10]The code used to implement all distance metrics in this thesis was produced by the author.

In this context, the vibration frequencies of the molecule ω_i are determined by the eigenvalues of the Laplacian matrix (4.1) via the equation $\lambda_i = \omega_i^2$ (where $\lambda_0 = \omega_0 = 0$).

In order to determine the spectral distance between two graphs, we introduce the following definition.

Definition 4.2.1. The *spectral density* of a graph is defined by

$$\rho(\omega, \gamma) = K \sum_{i=1}^{N-1} \frac{\gamma}{\gamma^2 + (\omega - \omega_i)^2}, \tag{4.4}$$

where γ is the scale parameter specifying the half-width at half-maximum (HWHM) of the Lorentz distribution, and K is the normalisation constant determined by

$$\int_0^\infty \rho(\omega, \gamma) \, d\omega = 1. \tag{4.5}$$

The Ipsen-Mikhailov distance is defined by comparing the spectral densities of two graphs.

Definition 4.2.2. The *Ipsen-Mikhailov distance*, or spectral distance, between two graphs, G and $\bar{G}$, is defined by

$$\epsilon_\gamma(G, \bar{G}) = \sqrt{\int_0^\infty [\rho_G(\omega, \gamma) - \rho_{\bar{G}}(\omega, \gamma)]^2 \, d\omega}. \tag{4.6}$$

We note that since all of our networks are formed of 98 ROIs, we do not need to consider a normalisation factor to account for differing numbers of nodes of the graphs, as in Jurman et al. [63]. Finally, we set $\gamma = 1/\pi$ such that the Ipsen-Mikhailov distance between and empty graph and complete graph is 1, as suggested by Jurman et al. [64].

4.2.2 Spanning tree dissimilarity

An alternative approach to assessing how the overall structure of a graph transforms between time windows is the spanning tree dissimilarity. In this method, the number of spanning trees of the networks is compared. The intuition lies in the idea that two graphs are viewed to be more distinctive if the transformation from one graph to another either creates or destroys a large number of spanning trees.

Kirchhoff's Matrix Tree Theorem gives us a way to calculate the number of spanning trees of a given connected network[11].

---

[11]See Harary [65] for further discussion.

Theorem 4.2.1 (The Matrix Tree Theorem). *Given a connected graph G with Laplacian L, the number of spanning trees of G, denoted $\tau(G)$, is equal to the value of each cofactor of the Laplacian of G.*

A corollary of this theorem provides a convenient way to calculate the number of spanning trees via the eigenvalues of the Laplacian[12].

Corollary 4.2.1.1. *Given a graph G, formed of N nodes, and its Laplacian L, the number of spanning trees is given by*

$$\tau(G) = \frac{1}{N} \prod_{i=1}^{N-1} \lambda_i, \tag{4.7}$$

where λ_i for $i = 1, 2, \ldots, N-1$ are the non-zero eigenvalues of L.

This corollary enables us to define another global metric.

Definition 4.2.3. The *spanning tree dissimilarity* between two graphs, G and $\bar{G}$, is defined by

$$d_{\text{span}}(G, \bar{G}) = |\log(\tau(G)) - \log(\tau(\bar{G}))|. \tag{4.8}$$

Proceeding by calculating the mean across subjects matrix for each frequency band, we plot the mean distance across all subjects between the network of time window 1 and time window t ($t = 2, 3, \ldots, 28$). This is seen in Figure 4.2 for the Ipsen-Mikhailov and spanning tree dissimilarity methods. Although the figure seems to suggest the distances between time windows vary randomly for both metrics, there are two features worth mentioning. Firstly, the bands with the lower frequencies tend to have the largest distances between networks of different time windows, with delta having the largest and the two gamma bands having the smallest. This suggests that there is a different level of overall graph transformation between the networks of different frequencies. Secondly, both of the approaches seem to display the same pattern for each frequency band across time windows. Therefore, it is clear that although these approaches are calculated in completely different ways, the methods capture the same levels of global transformation between time windows.

As discussed earlier, the adjacency matrices for the delta frequency band has the highest edge density, which may play a role in the relatively large distances between networks. However, the other frequency bands do not seem to follow a similar trend regarding the edge densities of the adjacency matrices. We investigate these properties further, along with similar properties of local approaches, in the next section.

---

[12]See Duval et al. [66] for further discussion.

(a) Ipsen-Mikhailov   **(b)** Spanning tree dissimilarity
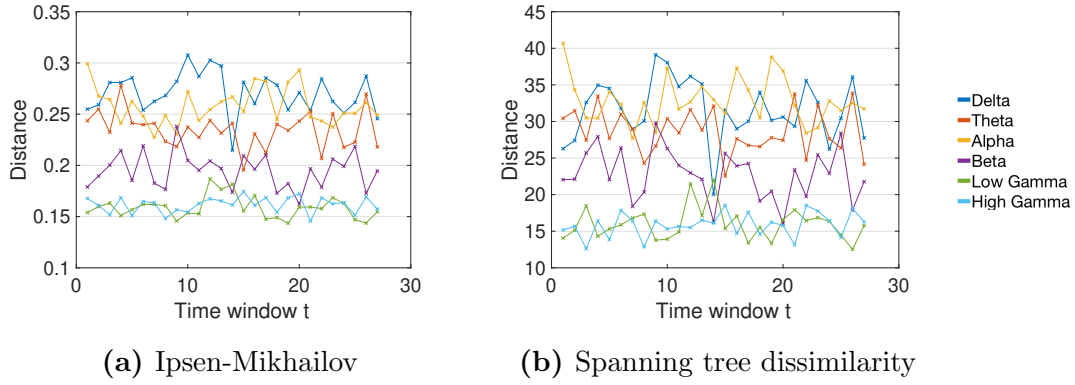
Figure 4.2: Global distance metrics for the mean of all subjects, measured between networks representing time window 1 and time window t ($t = 2, 3, \ldots, 28$).

We note here that if we use the thresholding function described by Meunier et al. [26] to form the adjacency matrices, then there will not necessarily be a path from each node to all other nodes. Therefore, these graphs will have no minimum spanning trees and thus, we are unable to define the spanning tree dissimilarity in this scenario.

Although global measures are useful for capturing a holistic view of the change between two graphs, they fail to capture information in the identities of the network nodes. Instead, we define structural distances, or 'local' approaches, to investigate changes at a more granular level.

4.3 Local approaches

4.3.1 Jaccard distance

The Jaccard distance is based on the Jaccard index between two edge sets, as introduced by Paul Jaccard [67], which is defined as the size of the intersection of two sets divided by the size of the union of the two sets

$$J(G, \bar{G}) = \frac{|G \cap \bar{G}|}{|G \cup \bar{G}|}. \tag{4.9}$$

Definition 4.3.1. The *Jaccard distance* between two graphs, G and $\bar{G}$, with corresponding adjacency matrices A and $\bar{A}$, is calculated as

$$
\begin{aligned}
d_{\text{Jaccard}}(G, \bar{G}) &= 1 - J(G, \bar{G}) \\
&= 1 - \frac{\sum_{i,j} \min(A_{ij}, \bar{A}_{ij})}{\sum_{i,j} \max(A_{ij}, \bar{A}_{ij})}.
\end{aligned}
\tag{4.10}
$$

33

Forming the mean across subjects matrix for each frequency band for the Jaccard distance, we then find the mean of all the elements of the matrix (excluding the main diagonal). This provides us with the mean pairwise distance between networks of all time windows for each band. This mean is displayed in Table 4.1. As can be seen from the table, the distance between time windows is dependent on frequency band, with the lower frequency bands tending to have a higher distance between networks for different time windows.

Frequency band	Jaccard distance
Delta	0.7059
Theta	0.6563
Alpha	0.6403
Beta	0.4422
Low gamma	0.4373
High gamma	0.3687

Table 4.1: Mean Jaccard distance, across all subjects, between all pairs of networks representing the 28 time windows.

This suggests that we are seeing a more drastic change in each of the ROIs' individual function for the lower frequencies. However, recalling that the brain is divided into functional systems, information on the role of individual nodes is not enough for interpreting brain dynamics. Additionally, the Jaccard distance is unable to reveal any interesting features about how the structural properties of the networks vary within each frequency band. This is because all of the elements within each matrix are very similar and close to the mean value displayed in the table (i.e. the pairwise Jaccard distances between networks of all time windows is very similar).

As with the global approaches, we use the analysis framework presented in Section 4.1 to plot the Jaccard distance between the graph of time window 1 and time window t ($t = 2, 3, \ldots, 28$) to see how the distance between graphs changes as the time between windows increases. We also plot the distance between time window t and time window $t + 1$ ($t = 1, 2, \ldots, 27$) to see how the distance between consecutive time windows changes. The results of this can be seen in Figure 4.3. The figure highlights the consistent distances between the time windows for a given frequency band. The figure also demonstrates the consistent differences in distances between networks of different frequency bands, with the higher frequency bands tending to have a smaller distance between the networks. The plots highlight the fact that we are seeing consistent levels of transformation across all time windows.

(a) Jaccard distance between time window 1 and t ($t = 2, 3, \ldots, 28$)

(b) Jaccard distance between time window t and t+1 ($t = 1, 2, \ldots, 27$)
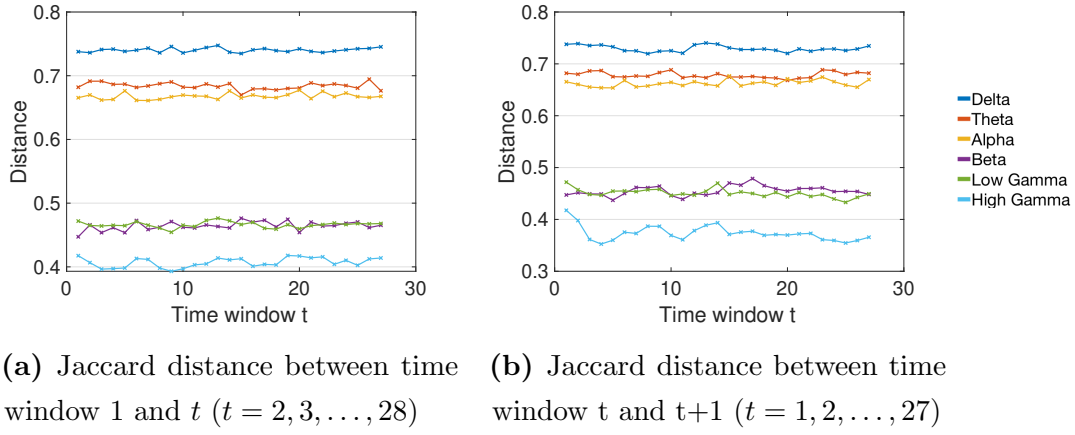
Figure 4.3: Mean Jaccard distance for all subjects between networks representing different time windows.

4.3.2 Hamming distance

The Hamming distance is another local approach that simply counts the difference between the number of edges of two graphs. Formally, this is defined as follows.

Definition 4.3.2. The *Hamming distance* between two graphs, G and $\bar{G}$, with adjacency matrices A and $\bar{A}$ respectively, is calculated as

$$d_{\text{Hamming}}(G, \bar{G}) = \frac{1}{N(N-1)} ||A - \bar{A}||_1, \tag{4.11}$$

where G and $\bar{G}$ both have N nodes.

In order to illustrate the similarities and differences between the global and local approaches in this section, we statistically analyse the mean distances across the 30 subjects. Taking the first row of each mean across subjects matrix as our data set, we are able to plot the boxplots in Figure 4.4 for each of the approaches. The figure confirms both the similarity of the two global approaches and the similarity of the two local approaches, but also highlights differences between the local and global approaches. We are able to see that the data for the local distances is tightly grouped with a much smaller interquartile range than the global approaches. On the other hand, the mean values of each of the frequency bands follow a similar pattern for all methods, highlighting a consistency in the effect of frequency of the band on the distance between networks of different time windows. The investigation into these types of properties helps our analysis in Chapter 5 as we explore sex differences in brain dynamics.

The primary drawback of the Jaccard and Hamming distances is that they focus on comparing the local information between two graphs, examining differences

35

(a) Ipsen-Mikhailov distance (global)

(b) Spanning tree dissimilarity (global)

(c) Jaccard distance (local)

(d) Hamming distance (local)
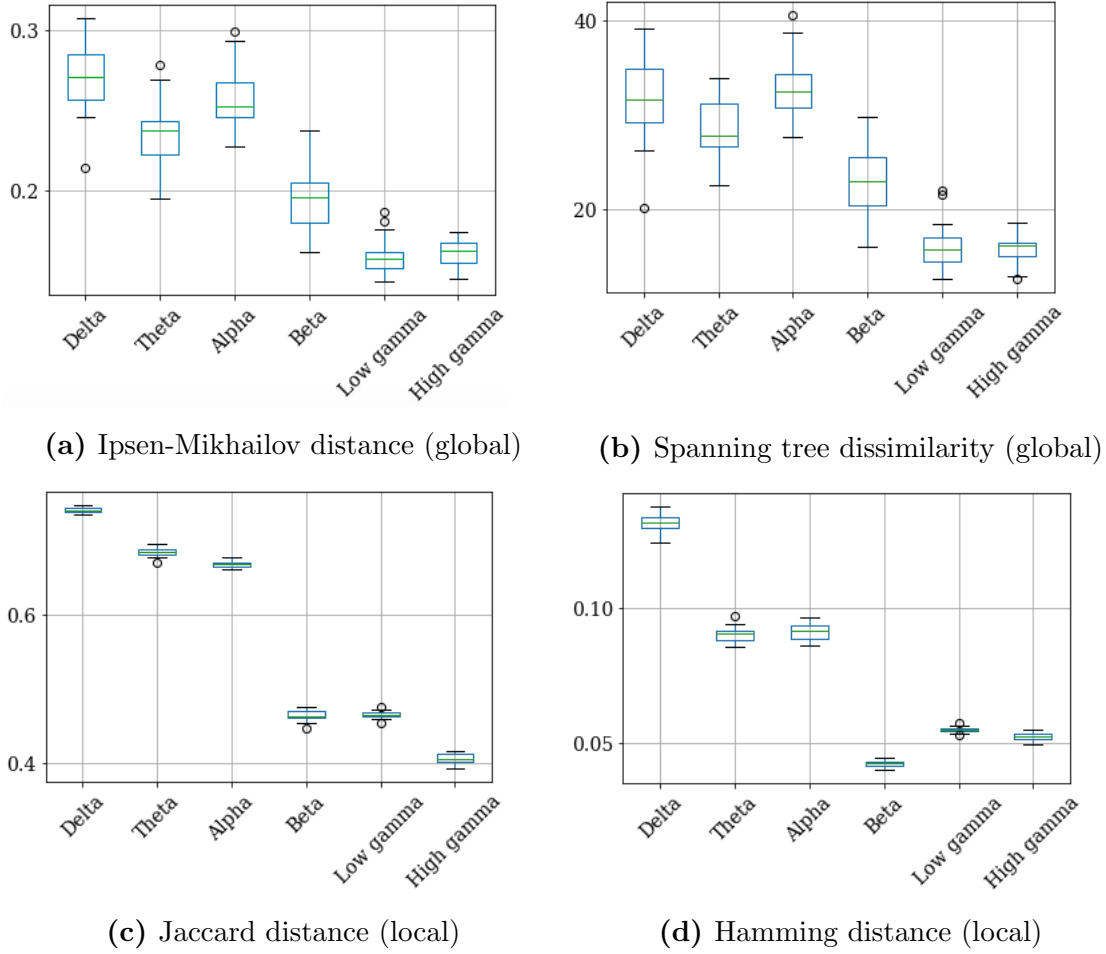
Figure 4.4: Boxplots for two global and two local distance metrics, made from the data of the mean distances, across all subjects, between networks of time window 1 and time window t $(t = 2, 3, \ldots, 28)$.

primarily at a node level, rather than considering effects on a complex system as a whole. However, by examining the eigenvalues of the adjacency matrix or a version of its Laplacian, global approaches are able to capture critical information at the entire network level. For our networks, we want to examine both the overall structure of the brain, as well as the dynamics of individual ROIs. Therefore, the goal is try to find approaches that can provide information across the spectrum, from node to whole network level.

One technique to do this is to combine a local and global approach. Proceeding in this way, we form the Hamming-Ipsen Mikhailov distance. Unfortunately, when we apply this method to our data, the HIM method does not seem to offer us any more information than the Ipsen-Mikhailov method (see Appendix C for a full discussion of the method). Another possible method is the polynomial approach,

which uses powers of the adjacency matrix A^k to calculate a new metric. Once again, in the particular case of our brain networks, the polynomial approach seems to offer little more than the Hamming distance, a local distance (see Appendix C for a full discussion of the method)[13]. Given that these approaches offer very little extra information to the local and global methods, we instead take a different approach and investigate mesoscale approaches. These approaches analyse graphs at the regional or neighbourhood level, which is suitable for our data considering the intrinsic functional systems of the brain.

4.4 Mesoscale approaches

Useful information about the properties of network transformations can often lie between the node and whole network level. For example, in brain connectome data, the information at the neuron level can be too noisy to gain any meaningful insight, but examining larger regions of the brain can shed light on important structural properties [30]. Mesoscale approaches offer this insight.

4.4.1 Heat spectral wavelets

In 2017, Donnat et al. [68] introduced a method, based on signal processing, to characterise the topological neighbourhood of each node of a graph. The approach assesses each node on the ability for a heat wavelet beginning at that node to diffuse through the network, as well as how the networks responds. Thus, this approach offers a more detailed view than a global approach, while also providing insight beyond nodal level changes.

Denote the Laplacian eigenvalue decomposition of an adjacency matrix by $L = U\Lambda U^T$, where $\Lambda = \text{diag}(\lambda_0, \ldots, \lambda_{N-1})$ and $0 = \lambda_0 \leq \lambda_1 \leq \ldots \leq \lambda_{N-1}$. The heat-scaling wavelet centred at node i with scale β, $\Psi_i^{(\beta)}$, is then defined as the ith column vector of $Ue^{-\beta\Lambda}U^T$, where $e^{-\beta\Lambda}$ is the diagonal matrix $\text{diag}(e^{-\beta\lambda_0}, e^{-\beta\lambda_1}, \ldots, e^{-\beta\lambda_{N-1}})$.

To assess how the wavelet affects the nodes across the network, Donnet et al. [68] defined the mth wavelet coefficient by

$$\Psi_{m,i}^{(\beta)} = \sum_{l=0}^{N-1} e^{-\beta\lambda_l} U_{il} U_{ml}. \tag{4.12}$$

Using this, the following metric can be defined.

---

[13]We include both methods in our male and female statistical analysis to see if the methods offer a new perspective when we divide the subject data into two groups.

Definition 4.4.1. The *heat spectral wavelet dissimlarity* between two graphs of N nodes, G_t and G_{t+1}, is defined by

$$d_{\text{hsw}}(G_t, G_{t+1}) = \frac{1}{N}\text{Tr}[\Delta^T\Delta], \tag{4.13}$$

where

$$\Delta = U_t e^{-\beta\Lambda_t} U_t^T - U_{t+1} e^{-\beta\Lambda_{t+1}} U_{t+1}^T.$$

The heat spectral wavelet dissimilarity metric highlights information about the connectedness and centrality of each ROI within the brain networks, with a large dissimilarity signifying a large volume of change [30]. Calculating the mean across subjects matrix for each frequency band, we plot the matrices as heatmaps in Figure 4.5. Unlike the Jaccard distance, the heat spectral wavelet dissimilarity between time windows shows a large degree of variability. For each frequency band, there are a select few time windows that display a higher dissimilarity to the other time windows. This implies that there are regional changes between these networks that aren't picked up by the local metrics, highlighting the benefit of mesoscale approaches.

4.4.2 Centrality dissimilarity

By considering the pairwise interactions between nodes of two graphs, we are able to define a connectivity-based dissimilarity metric determined by characterising nodes through a centrality measure.

Definition 4.4.2. The *centrality dissimilarity* between two graphs representing consecutive time windows, G_t and G_{t+1}, is calculated as

$$d_{\text{centrality}}(G_t, G_{t+1}) = \sqrt{\sum_{i=1}^{n}\left(b_i^{(t+1)} - b_i^{(t)}\right)^2}, \tag{4.14}$$

where $b_i^{(t)}$ is chosen to be the betweenness-centrality of node i at time t.

In Figure 4.6, the mean distance between networks representing time window 1 and time window t ($t = 2, 3, \ldots, 28$) for the centrality and heat spectral wavelet dissimilarities are plotted. Although a consistent distinction between the frequency bands can be seen, there does not seem to be the same trend relating to the frequency of the bands as there was with the local approaches. For both approaches, the beta frequency band displays the largest distances, suggesting more regional changes take

(a) Delta   **(b)** Theta   **(c)** Alpha

(d) Beta   **(e)** Low gamma   **(f)** High gamma
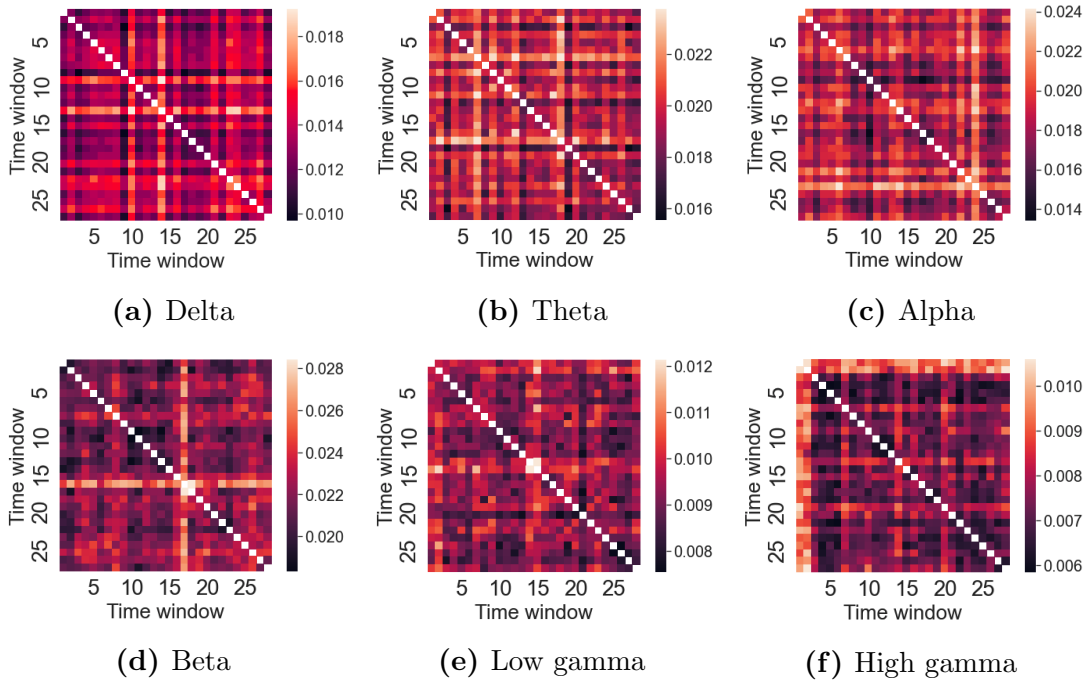
Figure 4.5: Heat spectral wavelet dissimilarity heatmaps for the mean of all subjects, using a scale of $\beta = 1.2$. Element (i, j) of each matrix represents the heat spectral wavelet dissimilarity between the network representing time window i and time window j. To satisfy the axioms of a metric, the main diagonal elements are all 0 and the matrices are symmetric.

place at this frequency band than the others. We note here that, as highlighted earlier in the chapter, the networks of each frequency band have different edge densities after applying the thresholding function. In particular, the networks of the beta frequency band have a much lower edge density than the other frequency bands, which could explain the notably high dissimilarities when applying mesoscale approaches.

4.5 Investigating the effect of edge densities

In order to test the effect of the edge densities, we want to investigate how changing the thresholding function affects the distance between networks of different time windows. This is done by applying the thresholding function used in Meunier et al. [26] (see Appendix B for full details of the method). For the thresholding function, we use a threshold value such that 3% of the total number of possible edges of the adjacency matrices are present. We then apply the metrics introduced throughout this chapter to the new adjacency matrices to calculate the distances between graphs

(a) Heat spectral wavelet   **(b)** Centrality dissimilarity
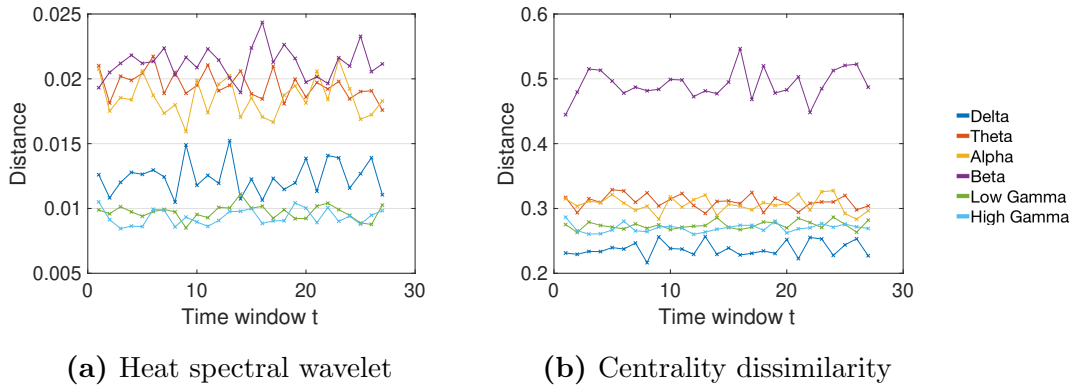
Figure 4.6: The mean heat spectral wavelet and centrality dissimilarities, across all subjects, between networks representing time window 1 and time window t ($t = 2, 3, \ldots, 28$). A scale of $\beta = 1.2$ is used for the heat spectral wavelet dissimilarity.

at time window 1 and time window t ($t = 2, 3, \ldots, 28$). The results are displayed in Figure 4.7.

As can be seen in the figure, the metrics show relatively similar results to the distances calculated using the thresholding function in Slater et al. [43]. The delta frequency band displays the largest distance between graphs once again for the Hamming, Jaccard, Ipsen-Mikhailov, Hamming-Ipsen-Mikhailov, and heat spectral wavelet metrics. As with the previous results, the low and high gamma frequency bands tend to show smaller distances between graphs. However, the figure highlights that with the updated thresholding function there is less of a distinction between theta, alpha, and beta frequency bands.

Finally, examining the graph for the centrality dissimilarity, it may appear that some frequency bands display cyclical behaviour across time windows. However, more investigation would be required to display evidence that the variability is anything more than noise. These results highlight that although we are able to witness general trends from the distance metrics, the thresholding method for creating the adjacency matrices can also play an important role.

After investigating the distance metrics on our subject data, the majority of the metrics point towards the data being fairly consistent between time windows. However, these metrics have enabled us to explore the differences between frequency bands at nodal, regional, and system level. In addition to the modular allegiance tools developed in Chapters 2 and 3, these techniques are extremely useful for investigating differences between male and female brains.

(a) Hamming

(b) Jaccard

(c) Ipsen-Mikhailov

(d) Haming-Ipsen-Mikhailov

(e) Centrality

(f) Heat spectral wavelet
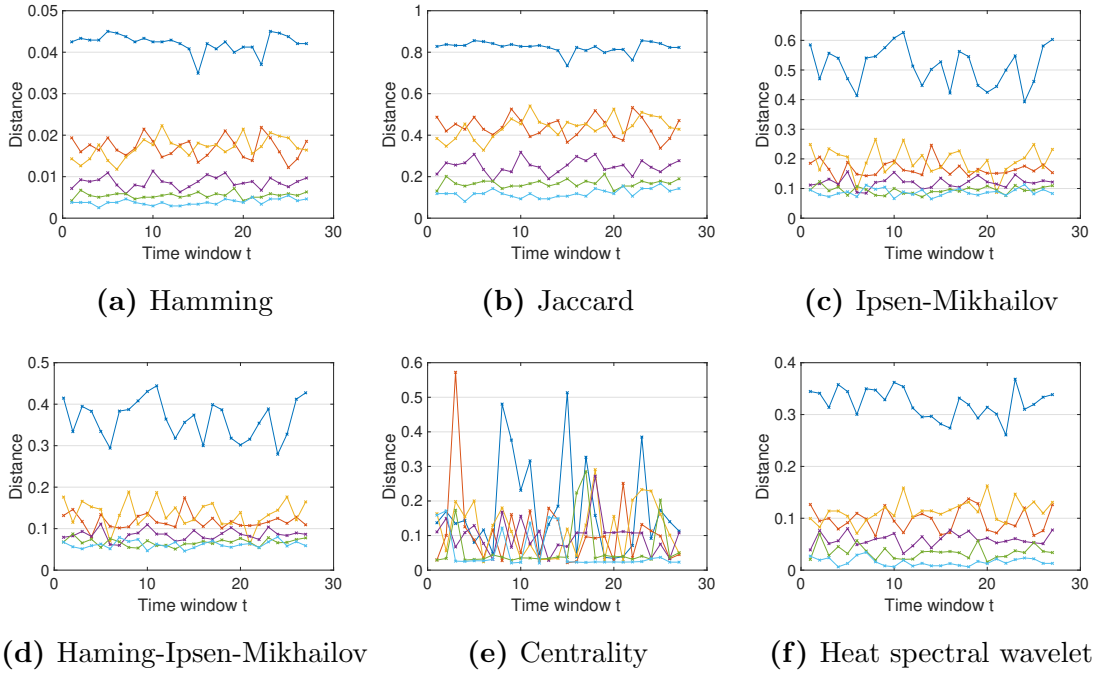
Figure 4.7: Mean distances of all subjects between time window 1 and time window t ($t = 2, 3, \ldots, 28$), for a number of distance metrics. The distances have been calculated from adjacency matrices formed using the thresholding function found in Meunier et al. [26]. A scale of $\beta = 1.2$ is used for the heat spectral wavelet dissimilarity. Frequency bands: delta (dark blue), theta (orange), alpha (yellow), beta (purple), low gamma (green), high gamma (light blue).

Chapter 5

Investigating sex differences in the human brain

This chapter aims to use the metrics developed throughout the earlier chapters to assess differences between male and female brains. We begin by performing some preliminary static modular analysis using tools from Chapter 2 to test for structural differences between male and female brains. We then proceed to utilise the dynamic modular allegiance metrics introduced in Chapter 3 to test for dynamical differences between the sexes across the time windows. Finally, we calculate the distances between graphs of different time windows for both sexes, using the metrics introduced in Chapter 4, in order to assess if the brains of each group change differently over the recorded time period.

5.1 Static modular analysis

In order to test for topological differences between male and female brain networks, we find the mean of the functional connectivity matrices across time windows for each subject. We then divide the 30 brain networks into the 15 male and 15 female subjects. By running the Louvain algorithm on each of the networks to find a natural partitioning, we are then able to compare the 15 values of modularity for each of the sexes. The difference in the mean of these two groups is calculated, and a permutation test with 10,000 permutations is used to assess if this difference is significant.

Although the initial test highlighted a significant difference in modularity ($p < 0.05$ uncorrected), when we applied a FDR-correction for testing against multiple frequency bands, the results were insignificant (full breakdown of results can be seen in Table D.3

(a) Female   (b) Male
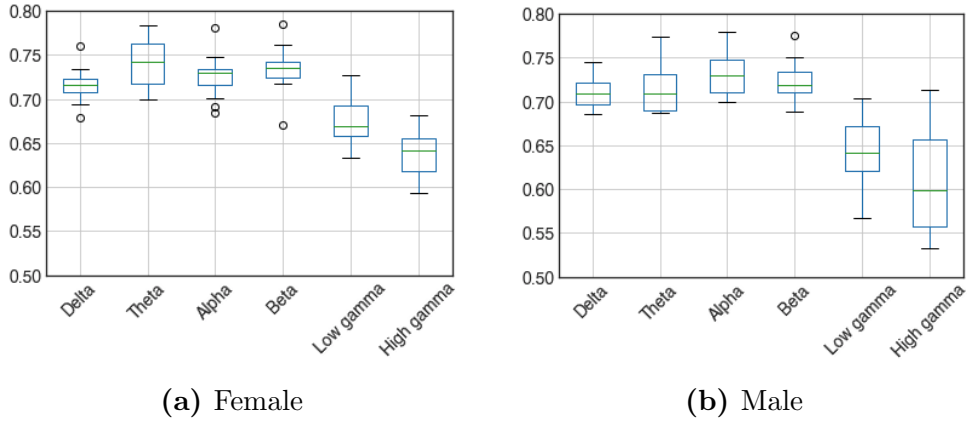
Figure 5.1: Boxplots showing the difference in the modularity of the male and female brain networks across frequency bands.

in Appendix D). This suggests that neither the male nor female brains are significantly more segregated or integrated than the other. Figure 5.1 displays statistical analyses of the male and female modularity values, highlighting the similarities between sexes. Agreeing with the analysis in Chapter 2, the low and high gamma frequency bands have a lower modularity value for both male and female subjects.

As with the modularity values, we are able to use the NMI between two networks to test for differences in modular partitions between male and female brains networks. When we test two groups with this method, we would expect two distinct groups to have a higher *within group* pairwise similarity than a *between group* pairwise similarity. However, we are unable to test this because the individual similarity measures are not independent. In order to test this, therefore, we use a permutation procedure that compares the mean within group similarity in the actual data with permutations where the group memberships are randomly permuted.

The permutation test is done by performing 10,000 permutations, comparing the average within group pairwise similarity in the actual data with permutations where the male and female data are mixed randomly. The p-value is then the proportion of the 10,000 trials for which the within group similarity is greater than the within group similarity of the actual data. If the actual within group similarity is greater than the permuted within group similarity for a large proportion of the permutations, this suggests the modular partition is related to sex.

Similar to the assessment of modularity, the assessment of the difference in community structures between the male and female brains highlighted no significant results ($p > 0.1$ uncorrected for all frequency bands; see Table D.4 in Appendix D for full breakdown of results). These two tests of the static modularity of the brains

suggest the structural properties of male and female brains are not significantly different. This result seems consistent with previous research, since globally we expect that modular structure is the same between both sexes. However, we hypothesise that differences are possibly more local, or in the dynamic communication between systems. We therefore use tools from dynamic analysis to explore these differences.

5.2   Dynamic modular analysis

In order to test for dynamical differences between male and female brains, we treat the 28 graphs formed from each of the time windows as slices of a multislice network. Performing the analysis presented in Chapter 3 on each of the subjects individually, the male and female subjects are then grouped to allow for comparison.

We begin by analysing the metrics that were measured for each individual ROI, but instead of analysing at node level to try to find specific ROI differences, we start at the whole network level to discover if there are broader dynamic differences. In order to do this, we find the sum of each network's recruitment, integration, flexibility, and promiscuity values, and then compare the mean of these values for the male and female subjects. This is done via a permutation test with 10,000 permutations. Even before a multiple comparison correction, we see no significant results across all four measures and six frequency bands ($p > 0.1$ for all results; see Table D.5 in Appendix D for the full breakdown of results). This suggests both male and female brains show similar levels of total recruitment, integration, flexibility and promiscuity across the time windows. Therefore, we examine the networks at a more detailed level to see if there are differences at the functional system level.

Beginning with the system level flexibility and promiscuity, we want to investigate if there are differences between the mean values of the male and female subjects. We once again use a permutation test with 10,000 permutations to investigate the difference. The p-value is simply the number of times that the permuted group of females and males has a mean flexibility or promiscuity which is greater than the actual data, divided by the number of permutations. Running the permutation test for the system level flexibility, we only find a significant difference for the sensorimotor system at the high gamma frequency band ($p = 0.0491$ uncorrected; see Table D.6 in Appendix D for full breakdown of results). However, applying a Bonferonni correction makes this result insignificant. Additionally, the permutation test for the system level promiscuity finds a significant difference for the subcortical system at the theta frequency band ($p = 0.0414$ uncorrected) and for the frontoparietal system at the low

gamma frequency band ($p = 0.0344$ uncorrected; see Table D.7 in Appendix D for full breakdown of results). However, both results were insignificant when corrected for multiple comparisons using a Bonferroni correction.

Using the normalised system modular allegiance matrices as calculated in Section 3.5, we want to test for differences in dynamics of the seven functional systems. We do this by testing for a difference in the 7 recruitment values of the systems and the 21 pairwise integration values between the systems for females and males. We once again perform a permutation test with 10,000 permutations to test the difference in the mean recruitment and integration values across the male and female subjects. The p-value is simply the number of times that the permuted group of males and females has a mean recruitment or integration value which is greater than the actual data, divided by the number of permutations.

Without correcting for multiple comparisons, we find a significant difference between male and female brains for the following pairwise integration between systems: delta - visual/salience ($p = 0.0131$); theta - visual/salience ($p = 0.0010$), visual/sensorimotor ($p = 0.0076$); alpha - visual/sensorimotor ($p = 0.0483$); high gamma - visual/auditory ($p = 0.0448$). Applying a Bonferroni correction, we find that only the integration between the visual and salience systems for the theta frequency band is significantly different. In Figure 5.2, these results have been plotted as a heat matrix, where element (i, j) represents the p-value of the difference in recruitment/integration of the systems between male and female brains (see Tables D.8–D.13 in Appendix D for full breakdown of results).

5.3 Comparison of distance metrics

After applying the thresholding function found in Slater et al. [43] to all the functional connectivity matrices, we introduced metrics in Chapter 4 that could find distances, or dissimilarities, between networks representing different time windows for each subject. Splitting the subjects by sex, we are able to calculate the pairwise distances for the 28 time windows for each frequency band. We then find the average pairwise distances for each of the sexes. Forming the graphs of distances between time window 1 and time window t ($t = 2, 3, \ldots, 28$) as before, we are able to display the calculated metrics for the mean of the male and female subjects. In Figure 5.3, the results are displayed for the Hamming metric, as an example. To investigate the difference between sexes, we begin by comparing the mean distances across all time windows for each frequency band.
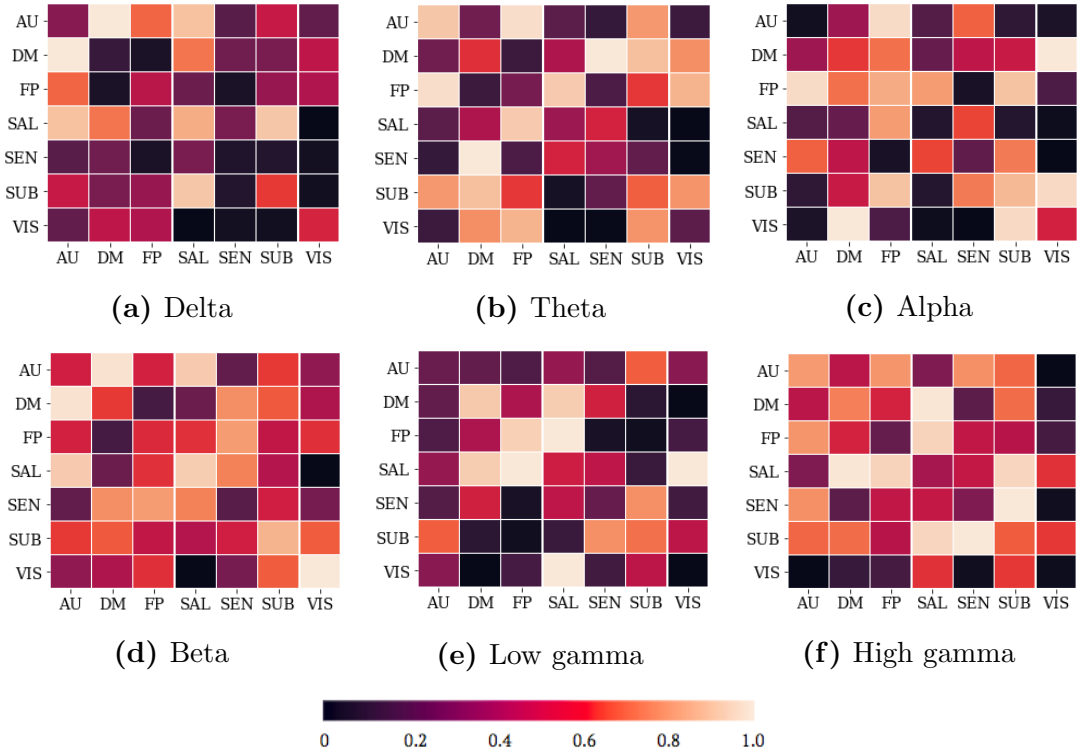
Figure 5.2: For each frequency band, element (i, j) represents the p-value of the difference in recruitment $(i = j)$ or integration of systems i and j between male and female brains. The difference is tested via 10,000 permutations of a permutation test. Functional system abbreviations: auditory (AU), default mode (DM), frontoparietal (FP), salience (SAL), sensorimotor (SEN), subcortical (SUB), visual (VIS).

In order to test for difference in means, we perform a t-test on the means of the two populations for each of the eight metrics and for each of the six frequency bands. Before applying a Bonferonni correction, significant differences were found for all metrics for the alpha, low gamma, and high gamma frequency bands. Significant differences were also found for five of the metrics for the beta and delta frequency bands, and six metrics of the theta band. Applying the Bonferonni correction, significant differences were still observed for all metrics of the alpha, low gamma, and high gamma frequency bands (see Table D.14 in Appendix D for full breakdown of results).

Given the limited number of subjects in our data set, we also performed a permutation test with 10,000 permutations in an attempt to verify the results found from the t-test. Before applying the Bonferonni correction, we once again witness a significant difference for all eight metrics across the alpha, low gamma and high

46

(a) Male

(b) Female
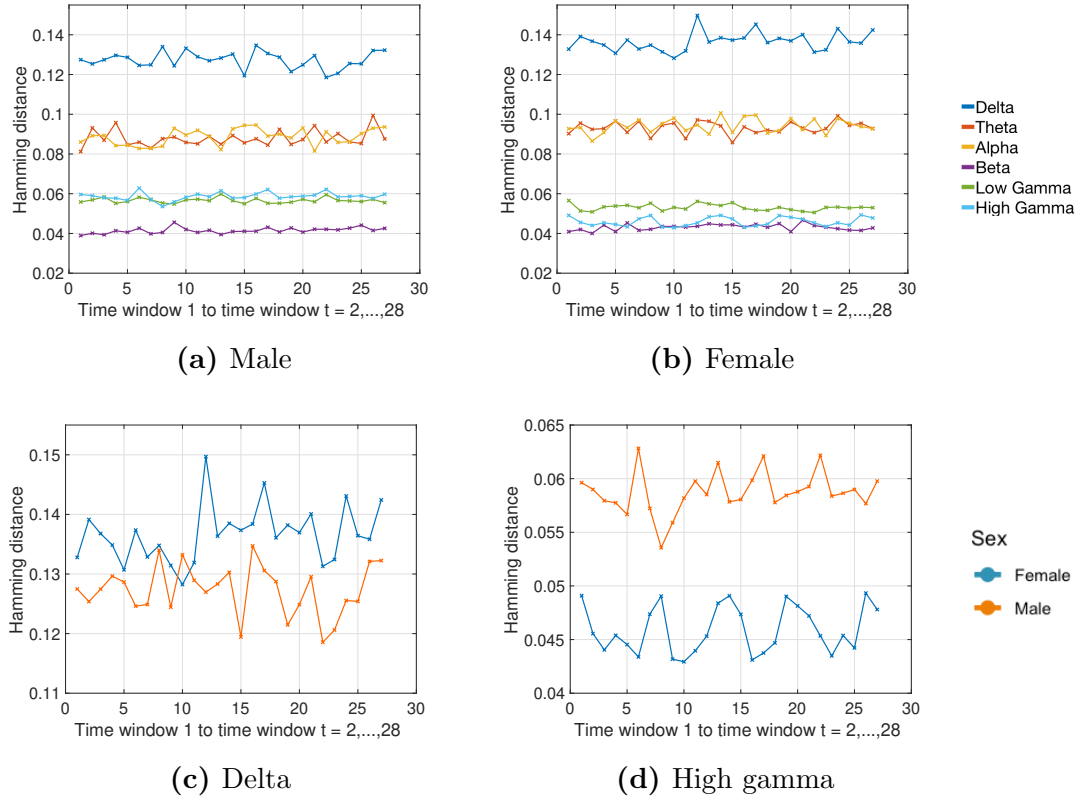
(c) Delta

(d) High gamma

Figure 5.3: (a, b) The mean Hamming distance across all subjects for the distances between time window 1 and t ($t = 2, 3, \ldots, 28$), for male and female subjects. **(c, d)** We display the results for both sexes for the delta and high gamma frequency bands to illustrate that networks from different bands transform by different amounts for each sex.

gamma frequency bands and for the majority of metrics for the theta and beta bands. After applying the Bonferonni correction, we still see significant differences for six or more metrics for the alpha, low gamma, and high gamma frequency bands. We see less significant differences for the lower frequency bands, delta and theta (see Table D.15 in Appendix D for full breakdown of results).

Overall, it is clear that male and female brains display distinct differences when we evaluate the distances between networks of different time windows for several of the selected metrics. This is true across the frequency bands, particularly for the higher frequency bands. Although the difference may not seem apparent from Figures 5.3b and 5.3a, we plot the same results but only for the delta and high gamma frequency band for both the females and males on the same graph in Figures 5.3c and 5.3d. Examining the figure, it is clear that the distances of the two sexes are

very different across time windows, explaining why we find a significant difference.

In order to further understand these differences, we take a closer look at which sex displayed larger values for each of the metrics. For the theta, beta, low gamma, and high gamma frequency bands, we see that the male networks display larger distances for six or more of the eight metrics. On the other hand, for the delta and alpha frequency bands, the female networks display larger values for seven or more of the metrics. This highlights a very distinct difference between the frequency bands for each sex, with a general trend that the higher frequency bands displayed greater transformations between networks for males than females.

In general, this difference in the distance between networks for each of the sexes implies the networks are undergoing different levels of transformation between time windows. To understand more about what this difference means, and therefore understand more about the way that the sexes differ, we look to the meaning behind three of the metrics (one global, one local, and one mesoscale approach).

The spanning tree dissimilarity metric was inspired by Kelmans [69], who described the transformation between two graphs by their 'ability to destroy' spanning trees. In the context of brain networks, the transformations of the female networks show a consistently high 'ability to destroy' when compared to the transformations of the male networks for the delta and alpha frequency bands. The number of spanning trees that a network has is essentially a measure of the graph's interconnectedness. Therefore, we are seeing a significant difference in the change of the interconnectedness of the networks of the two sexes.

The Hamming metric counts the difference between the number of edges of two graphs. Examining the metric more closely, we realise that this is a measure of both the number of edges that are deleted and inserted during the transformation. Interestingly, the difference between the frequency bands of the two sexes follows a different pattern to the other metrics. For the delta, theta, alpha, and beta bands, the female subjects display a significantly larger Hamming distance between networks than the males. This suggests that for the lower frequency data, the female networks show a consistently larger number of edge changes than the male networks. However, as the frequency increases to the levels of low and high gamma, the male subjects display a significantly larger Hamming distance between networks of different time windows.

For the centrality dissimilarity, a mesoscale approach, the betweenness centrality measure was chosen. A centrality measure essentially measures the importance of each node within a network. In this particular case, the betweenness centrality

measures the proportion of shortest paths between all pairs of nodes that pass through each node. Therefore, the centrality dissimilarity metric measures the change in the roles of the nodes. Once again, the networks for the female subjects show larger distances between each other when compared to male networks for the delta and alpha bands. This suggests a greater change between the interactions of the networks is happening for the female subjects at these frequencies.

Finally, we compare variances to see if we experience larger variability in distances between networks for one sex compared to the other. Using a Levene's test to assess the equality of variances between the two sets of data, the results found that the spanning tree dissimilarity ($F = 4.529$, $p = 0.0381$ uncorrected), Ipsen-Mikhailov ($F = 4.569$, $p = 0.0373$ uncorrected), and Hamming-Ipsen-Mikhailov ($F = 4.403$, $p = 0.0407$ uncorrected) were significantly different for the theta frequency band. Additionally, a significant difference was found for the polynomial metric ($F = 4.076$, $p = 0.0487$ uncorrected) for the high gamma frequency band. However, applying a Bonferroni correction suggested these differences were insignificant (see Table D.16 in Appendix D for full breakdown of results). This means that although there appears to be significant differences in the mean value of the distances between time windows, the variance of the distances appears to be similar between sexes.

Chapter 6

Conclusion

6.1 Summary

Network neuroscience has proven pivotal in developing neuroscientists' understanding of the brain. Recent innovation in brain imaging methods has garnered vast amounts of interest in applying mathematical techniques to neuroscience. With the potential to provide earlier diagnosis of diseases and find predictors of treatment outcome, as well as explore fascinating concepts regarding personality traits and brain structure, it is clear the field will continue to grow and gain prominence.

Preprocessing MEG data obtained from the HCP Young Adult study enabled us to form networks representing the brain that could be analysed to explore its structural and dynamical properties. The main focus of this thesis was to explore a selection of metrics to aid this investigation, and apply them in the context of comparing male and female brains of subjects in their resting-state. By taking the mean of the functional connectivity matrices for each subject across the 28 time windows, we were able to use the Louvain algorithm to find communities representing the structural properties of the brains.

Given the strong temporal resolution of MEG data, we were able to compare the modularity and community partitions of networks representing different frequency bands. This highlighted a distinct difference between the static organisation of the brain at different frequencies. The networks of the low and high gamma frequency bands showed a distinctly lower modularity and pairwise NMI. It is known that the different frequency brain waves sustain different functions and states of the brain; our results supported this by highlighting that different brain architecture was shown for the lower and higher frequency bands (i.e. they are structurally different).

Building on the static analysis, we treated the networks representing different time

windows as slices of a multislice network and used dynamic modular analysis to assess community assignment. Introducing four metrics to assess community dynamics (flexibility, promiscuity, recruitment, integration), we discovered that the bands of higher frequency tended to have higher recruitment and integration values, yet lower flexibility and promiscuity values. Our analysis found that nodes of the auditory and visual systems were relatively stable, and stayed in their respective systems across time windows, as highlighted by their high recruitment values. Additionally, the low integration between these two systems suggested that their ROIs did not interact frequently across time windows. This result is consistent with the anatomical proximity of the ROIs of the visual sensory system, which are all located in the rear of the cortex. Visual information processing mainly relies on connections within the visual system, which may explain the high recruitment in our results.

Investigating network dynamics from an alternative viewpoint, we calculated a number of distance metrics between networks representing different time windows. Introducing global, local, and mesoscale approaches enabled us to examine the network transformations from a variety of perspectives. We noticed that the networks of the higher frequency bands tended to have a smaller distance between them when analysed using the global and local approaches. The exception to this trend was the beta frequency band. However, it was shown that when the thresholding function was applied to the networks of the beta band, the density of the resulting adjacency matrices was relatively low. Therefore, we repeated the analysis with a different thresholding function, which produced networks with a consistent edge density. The results then highlighted a consistent trend, with the bands of lower frequency having larger distances between networks of different time windows. This highlighted the importance of choosing a suitable thresholding function.

To the best of our knowledge, these metrics have not been applied to brain MEG data in order to investigate brainwaves of different frequencies. Therefore, by taking advantage of the improved temporal resolution of MEG imaging, we have been able to shed new light on the different dynamic brain properties at different frequencies. In particular, we have been able to contribute to the field by using these metrics to investigate the difference between male and female brains.

By exploring a wide range of static and dynamic analyses, we have been able to assess the difference between male and female resting-state brain data. Performing the static modular analysis uncovered no significant differences between the sexes, suggesting that globally there is little to distinguish the modular structures of the brains of the two sexes. Similar results were displayed when we applied the

dynamic methods developed in Chapter 3. However, one noticeable difference was the integration between the visual and salience systems, where the female subjects displayed a much higher integration than the male subjects ($p = 0.001$ Bonferonni corrected) for the theta frequency band.

Finally, applying the distance metric tools developed in Chapter 4, we discovered vast differences between male and female brains. In particular, analysing the mean distance between networks representing time window 1 and time window t ($t = 2, 3, \ldots, 28$), there was a clear difference between the distances of the male and female brain networks. Examining this more closely, we noticed that for the majority of the metrics, there was a larger distance between male networks of different time windows for the theta, beta, low gamma, and high gamma frequency bands. However, for the delta and alpha bands, there was a larger distance between the female networks. This highlighted that, between the sexes, there is a difference in the level of transformation of the structure of the brains at different frequencies.

In conclusion, by investigating the brain organisation of healthy people during resting-state, our analysis showed that the intrinsic systems of the brain have different static and dynamic organisation according to the brain waves considered (high vs low frequency bands). Notably, these dynamical topological properties are substantially influenced by sex differences. A better understanding of these innate brain differences between the sexes may help to isolate specific abnormalities related to conditions in patients.

Altogether, the present results suggest that brain studies that do not examine data for both sexes separately may risk bias in interpreting their findings. They may also be at risk of missing important information and, in the case of single sex studies, may have limited generalisability [70]. Thus, the technical and methodological approach developed in this thesis provides a framework to understand sex differences in the brain using recent mathematical and neuroscientific techniques.

6.2 Future work

There are a number of possibilities for future work that can stem from this thesis.

Structural investigation of temporal frequencies: Due to the improved temporal resolution that MEG data provides, our results highlighted that lower and higher frequency bands displayed different brain modular organisation. Given that each frequency band displays different brain state characteristics, it would be worthwhile to investigate how the brain is organised for each frequency band while performing tasks characterising each band. This could show how each band is organised while performing its primary function, as well as while it is less active.

Application of thresholding function: The choice of thresholding function to convert connectivity matrices to adjacency matrices is mixed in the literature, and is seemingly arbitrary. In order to simplify our approach, and test new methods on MEG data, we set negative correlations to 0. However, in resting-state, brain subsystems may be anti-correlated with each other [71], and the sign of correlations in graph analysis permits the segregation of anti-correlated subsystems [72]. In addition, negative correlations between activities also play an important role in explaining cognitive processes [73]. Therefore, it is important in future investigations to consider the sign of correlation coefficients.

Further investigation of demographics: An important extension of this work would be to confirm and explore the distance metrics results. Many researchers have claimed to find differences between male and female brains, yet further probing has often found the results to be insignificant or incorrect. By introducing more subjects, further work could validate our results, providing a platform from which to investigate the causes and implications of these differences. Additionally, applying our framework to more subjects will allow for an investigation into the difference between subjects of different demographics (e.g. race, age), or subjects diagnosed with brain disorders. This could potentially lead to an explanation of why certain disorders are more common in some demographics than others.

Bibliography

[1]   Mark EJ Newman. "The structure and function of complex networks". In: *SIAM review* 45.2 (2003), pp. 167–256.

[2]   Stefano Boccaletti et al. "Complex networks: Structure and dynamics". In: *Physics reports* 424.4-5 (2006), pp. 175–308.

[3]   Sergei N Dorogovtsev and José FF Mendes. *Evolution of networks: From biological nets to the Internet and WWW*. OUP Oxford, 2013.

[4]   Alex Fornito, Andrew Zalesky, and Edward Bullimore. *Fundamentals of Brain Network Analysis*. 2016.

[5]   S Finger. "Paul Broca (1824-1880)". In: *Journal of Neurology* 251.6 (2004), p. 769.

[6]   Julien Dubois et al. "Resting-state functional brain connectivity best predicts the personality dimension of openness to experience". In: *Personality neuroscience* 1 (2018).

[7]   Gary H Glover. "Overview of functional magnetic resonance imaging". In: *Neurosurgery Clinics* 22.2 (2011), pp. 133–139.

[8]   Pawel Skudlarski et al. "Brain connectivity is not only lower but different in schizophrenia: a combined anatomical and functional approach". In: *Biological psychiatry* 68.1 (2010), pp. 61–69.

[9]   Mary-Ellen Lynall et al. "Functional connectivity and brain networks in schizophrenia". In: *Journal of Neuroscience* 30.28 (2010), pp. 9477–9487.

[10] Nam P Nguyen et al. "Dynamic social community detection and its applications". In: *PloS one* 9.4 (2014), e91431.

[11] Michelle Girvan and Mark EJ Newman. "Community structure in social and biological networks". In: *Proceedings of the national academy of sciences* 99.12 (2002), pp. 7821–7826.

[12] Till Hoffmann et al. "Community detection in networks without observing edges". In: *Science advances* 6.4 (2020), eaav1478.

[13] Karolina Finc et al. "Dynamic reconfiguration of functional brain networks during working memory training". In: *bioRxiv* (2019). DOI: 10.1101/685487. eprint: https://www.biorxiv.org/content/early/2019/06/27/685487.full.pdf. URL: https://www.biorxiv.org/content/early/2019/06/27/685487.

[14] Marcelo G. Mattar et al. "A Functional Cartography of Cognitive Systems". In: *PLOS Computational Biology* 11.12 (Dec. 2015), pp. 1–26. DOI: 10.1371/journal.pcbi.1004533. URL: https://doi.org/10.1371/journal.pcbi.1004533.

[15] Danielle S Bassett et al. "Learning-induced autonomy of sensorimotor systems". In: *Nature neuroscience* 18.5 (2015), pp. 744–751.

[16] Emily S Finn et al. "Functional connectome fingerprinting: identifying individuals using patterns of brain connectivity". In: *Nature neuroscience* 18.11 (2015), pp. 1664–1671.

[17] Aaron Alexander-Bloch et al. "The discovery of population differences in network community structure: New methods and applications to brain functional networks in schizophrenia". In: *NeuroImage* 59.4 (2012), pp. 3889–3900. ISSN: 1053-8119. DOI: https://doi.org/10.1016/j.neuroimage.2011.11.035. URL: http://www.sciencedirect.com/science/article/pii/S1053811911013164.

[18] Kaat Alaerts, Stephan P Swinnen, and Nicole Wenderoth. "Sex differences in autism: a resting-state fMRI investigation of functional brain connectivity in males and females". In: *Social cognitive and affective neuroscience* 11.6 (2016), pp. 1002–1016.

[19] E Zagni, L Simoni, and D Colombo. *Sex and gender differences in central nervous system-related disorders. Neurosci J. 2016; 2016: 2827090.*

[20] Stuart J Ritchie et al. "Sex differences in the adult human brain: evidence from 5216 UK Biobank participants". In: *Cerebral Cortex* 28.8 (2018), pp. 2959–2975.

[21] Martin Lotze et al. "Novel findings from 2,838 adult brains on sex differences in gray matter brain volume". In: *Scientific reports* 9.1 (2019), pp. 1–7.

[22]   Daphna Joel et al. "Sex beyond the genitalia: The human brain mosaic". In: *Proceedings of the National Academy of Sciences* 112.50 (2015), pp. 15468–15473.

[23]   Karen J Berkley. "Sex differences in pain". In: *Behavioral and Brain Sciences* 20.3 (1997), pp. 371–380.

[24]   Jeffrey S Mogil. "Sex differences in pain and pain inhibition: multiple explanations of a controversial phenomenon". In: *Nature Reviews Neuroscience* 13.12 (2012), pp. 859–866.

[25]   Dilansu Guneykaya et al. "Transcriptional and translational differences of microglia from male and female brains". In: *Cell reports* 24.10 (2018), pp. 2773–2783.

[26]   David Meunier et al. "Age-related changes in modular organization of human brain functional networks". In: *NeuroImage* 44.3 (2009), pp. 715–723. ISSN: 1053-8119. DOI: https://doi.org/10.1016/j.neuroimage.2008.09.062. URL: http://www.sciencedirect.com/science/article/pii/S1053811908011026.

[27]   Jennifer Rizkallah et al. "Dynamic reshaping of functional brain networks during visual object recognition". In: *Journal of Neural Engineering* 15 (Aug. 2018). DOI: 10.1088/1741-2552/aad7b1.

[28]   Yoon Jae Kim et al. "A study on a robot arm driven by three-dimensional trajectories predicted from non-invasive neural signals". In: *Biomedical engineering online* 14.1 (2015), p. 81.

[29]   Aya Kabbara et al. "Brain network dynamics correlate with personality traits". In: *Brain connectivity* 10.3 (2020), pp. 108–120.

[30]   Claire Donnat and Susan Holmes. *Tracking network dynamics: a survey of distances and similarity metrics.* 2018. arXiv: 1801.07351 [stat.AP].

[31]   Kamil Ugurbil and David Van Essen. *Human Connectome Project.* https://www.humanconnectome.org/study/hcp-young-adult. Mar. 2017.

[32]   Jayabal Velmurugan, Sanjib Sinha, and Parthasarathy Satishchandra. "Magnetoencephalography recording and analysis". In: *Annals of Indian Academy of Neurology* 17.Suppl 1 (2014), S113.

[33]   Junseok A Kim et al. "Neuropathic pain and pain interference are linked to alpha-band slowing and reduced beta-band magnetoencephalography activity within the dynamic pain connectome in patients with multiple sclerosis". In: *Pain* 160.1 (2019), pp. 187–197.

[34]   Lee B Kisler et al. "Abnormal alpha band power in the dynamic pain connectome is a marker of chronic pain with a neuropathic component". In: *NeuroImage: Clinical* (2020), p. 102241.

[35]   Barry D Van Veen et al. "Localization of brain electrical activity via linearly constrained minimum variance spatial filtering". In: *IEEE Transactions on biomedical engineering* 44.9 (1997), pp. 867–880.

[36]   Arjan Hillebrand et al. "A new approach to neuroimaging with magnetoencephalography". In: *Human brain mapping* 25.2 (2005), pp. 199–211.

[37]   Yicheng Long et al. "Psychological resilience negatively correlates with resting-state brain network flexibility in young healthy adults: a dynamic functional magnetic resonance imaging study". In: *Annals of Translational Medicine* 7.24 (2019). ISSN: 2305-5847. URL: http://atm.amegroups.com/article/view/33383.

[38]   Zhongming Liu et al. "Large-scale spontaneous fluctuations and correlations in brain electrical activity observed with magnetoencephalography". In: *Neuroimage* 51.1 (2010), pp. 102–111.

[39]   Giles L Colclough et al. "A symmetric multivariate leakage correction for MEG connectomes". In: *Neuroimage* 117 (2015), pp. 439–448.

[40]   Jiří Lebl. *Introduction to Real Analysis, Volume I*. 2018.

[41]   Vincent A Traag and Jeroen Bruggeman. "Community detection in networks with positive and negative links". In: *Physical Review E* 80.3 (2009), p. 036115.

[42]   Sophie Achard et al. "A resilient, low-frequency, small-world human brain functional network with highly connected association cortical hubs". In: *Journal of Neuroscience* 26.1 (2006), pp. 63–72.

[43]   P. B. Slater. "A two-stage algorithm for extracting the multiscale backbone of complex weighted networks". In: *Proceedings of the National Academy of Sciences* 106.26 (June 2009), E66–E66. ISSN: 1091-6490. DOI: 10.1073/pnas.0904725106. URL: http://dx.doi.org/10.1073/pnas.0904725106.

[44]   J.-C. Delvenne, S. N. Yaliraki, and M. Barahona. "Stability of graph communities across time scales". In: *Proceedings of the National Academy of Sciences* 107.29 (2010), pp. 12755–12760. ISSN: 0027-8424. DOI: `10.1073/pnas.0903215107`. eprint: `https://www.pnas.org/content/107/29/12755.full.pdf`. URL: `https://www.pnas.org/content/107/29/12755`.

[45]   EL-MOUSSAOUI Mohamed et al. "A comprehensive literature review on community detection: Approaches and applications". In: *Procedia Computer Science* 151 (2019), pp. 295–302.

[46]   Vincent D Blondel et al. "Fast unfolding of communities in large networks". In: *Journal of Statistical Mechanics: Theory and Experiment* 2008.10 (Oct. 2008), P10008. ISSN: 1742-5468. DOI: `10.1088/1742-5468/2008/10/p10008`. URL: `http://dx.doi.org/10.1088/1742-5468/2008/10/P10008`.

[47]   Vincent A Traag, Ludo Waltman, and Nees Jan van Eck. "From Louvain to Leiden: guaranteeing well-connected communities". In: *Scientific reports* 9.1 (2019), pp. 1–12.

[48]   William Hedley Thompson et al. "Time-varying nodal measures with temporal community structure: A cautionary note to avoid misinterpretation". In: *Human Brain Mapping* 41.9 (2020), pp. 2347–2356.

[49]   Kirsten Hilger et al. "Temporal stability of functional brain modules associated with human intelligence". In: *Human Brain Mapping* 41.2 (2020), pp. 362–372.

[50]   Kimberly J Schlesinger et al. "Improving resolution of dynamic communities in human brain networks through targeted node removal". In: *PloS one* 12.12 (2017), e0187715.

[51]   Mark Newman and Michelle Girvan. "Finding and Evaluating Community Structure in Networks". In: *Physical review. E, Statistical, nonlinear, and soft matter physics* 69 (Mar. 2004), p. 026113. DOI: `10.1103/PhysRevE.69.026113`.

[52]   Béla Bollobás. "A probabilistic proof of an asymptotic formula for the number of labelled regular graphs". In: *European Journal of Combinatorics* 1.4 (1980), pp. 311–316.

[53]   Ludmila Kuncheva and Stefan Hadjitodorov. "Using Diversity in Cluster Ensembles". In: vol. 2. Jan. 2004, pp. 1214–1219. DOI: `10.1109/ICSMC.2004.1399790`.

[54]   Priyanka A Abhang, Bharti W Gawali, and Suresh C Mehrotra. *Introduction to EEG-and speech-based emotion recognition*. Academic Press, 2016.

[55] Ann E. Sizemore and Danielle S. Bassett. "Dynamic graph metrics: Tutorial, toolbox, and tale". In: *NeuroImage* 180 (2018). Brain Connectivity Dynamics, pp. 417–427. ISSN: 1053-8119. DOI: https://doi.org/10.1016/j.neuroimage.2017.06.081. URL: http://www.sciencedirect.com/science/article/pii/S1053811917305645.

[56] Karolina Finc et al. *Dynamic reconfiguration of functional brain networks during working memory training.* Jan. 2020. DOI: 10.17605/OSF.IO/WF85U. URL: osf.io/wf85u.

[57] Dani Bassett et al. *Network Community Toolbox.* http://commdetect.weebly.com/. Accessed: 2020-06-30.

[58] P. J. Mucha et al. "Community Structure in Time-Dependent, Multiscale, and Multiplex Networks". In: *Science* 328.5980 (May 2010), pp. 876–878. ISSN: 1095-9203. DOI: 10.1126/science.1184819. URL: http://dx.doi.org/10.1126/science.1184819.

[59] Lucas G. S. Jeub et al. *A generalized Louvain method for community detection implemented in MATLAB.* 2011–2019. URL: https://github.com/GenLouvain/GenLouvain.

[60] Lia Papadopoulos et al. "Evolution of network architecture in a granular material under compression". In: *Physical Review E* 94.3 (2016), p. 032908.

[61] Jing Huang and Shuchao Li. "On the normalised Laplacian spectrum, degree-Kirchhoff index and spanning trees of graphs". In: *Bulletin of the Australian Mathematical Society* 91.3 (2015), pp. 353–367.

[62] Mads Ipsen and Alexander S. Mikhailov. "Evolutionary reconstruction of networks". In: *Phys. Rev. E* 66 (4 Oct. 2002), p. 046109. DOI: 10.1103/PhysRevE.66.046109. URL: https://link.aps.org/doi/10.1103/PhysRevE.66.046109.

[63] Giuseppe Jurman et al. "Biological network comparison via Ipsen-Mikhailov distance". In: *arXiv preprint arXiv:1109.0220* (2011).

[64] Giuseppe Jurman et al. *The HIM glocal metric and kernel for network comparison and classification.* 2012. arXiv: 1201.2931 [math.CO].

[65] F. Harary. *Graph Theory.* Addison-Wesley Publishing Company, 1969.

[66] Art Duval, Caroline Klivans, and Jeremy Martin. "Simplicial matrix-tree theorems". In: *Transactions of the American Mathematical Society* 361.11 (2009), pp. 6073–6114.

[67]   Paul Jaccard. "Distribution de la Flore Alpine dans le Bassin des Dranses et dans quelques régions voisines." In: *Bulletin de la Societe Vaudoise des Sciences Naturelles* 37 (Jan. 1901), pp. 241–72. DOI: `10.5169/seals-266440`.

[68]   Claire Donnat et al. *Spectral Graph Wavelets for Structural Role Similarity in Networks*. 2018. URL: `https://openreview.net/forum?id=rJR2ylbRb`.

[69]   Alexander K Kelmans. "Transformations of a graph increasing its Laplacian polynomial and number of spanning trees". In: *European Journal of Combinatorics* 18.1 (1997), pp. 35–48.

[70]   Arpana Gupta et al. "Sex-based differences in brain alterations across chronic pain conditions". In: *Journal of neuroscience research* 95.1-2 (2017), pp. 604–616.

[71]   Michael D Fox et al. "The human brain is intrinsically organized into dynamic, anticorrelated functional networks". In: *Proceedings of the National Academy of Sciences* 102.27 (2005), pp. 9673–9678.

[72]   Mikail Rubinov and Olaf Sporns. "Weight-conserving characterization of complex functional brain networks". In: *Neuroimage* 56.4 (2011), pp. 2068–2079.

[73]   AM Clare Kelly et al. "Competition between functional brain networks mediates behavioral variability". In: *Neuroimage* 39.1 (2008), pp. 527–537.

[74]   Béla Bollobás. "The evolution of random graphs—the giant component". In: *Random Graphs*. Vol. 184. Cambridge University Press Cambridge. 2001, pp. 130–59.

Appendix A

AAL atlas of regions of interest

Index	Regions	Subnetwork Affiliation	x	y	z
1	Precental gyrus	Sensorimotor	-40	-6	51
2	Precental gyrus	Sensorimotor	40	-8	52
3	Superior frontal gyrus	Frontoparietal	-19	35	42
4	Superior frontal gyrus	Frontoparietal	20	31	44
5	Superior frontal gyrus	Frontoparietal	-18	47	-13
6	Superior frontal gyrus	Frontoparietal	17	48	-14
7	Middle frontal gyrus	Frontoparietal	-34	33	35
8	Middle frontal gyrus	Frontoparietal	37	33	34
9	Middle frontal gyrus	Default mode	-32	50	-10
10	Middle frontal gyrus	Default mode	32	53	-11
11	Inferior frontal gyrus	Salience	-49	13	19
12	Inferior frontal gyrus	Salience	49	15	21
13	Inferior frontal gyrus	Salience	-47	30	14
14	Inferior frontal gyrus	Salience	49	30	14
15	Inferior frontal gyrus	Default mode	-37	31	-12
16	Inferior frontal gyrus	Default mode	40	32	-12
17	Rolandic operculum	Auditory	-48	-8	14
18	Rolandic operculum	Auditory	52	-6	15
19	Supplementary motor area	Sensorimotor	-6	5	61
20	Supplementary motor area	Sensorimotor	8	0	62
21	Olfactory cortex	Subcortical	-9	15	-12
22	Olfactory cortex	Subcortical	8	16	-11
23	Superior frontal gyrus	Frontoparietal	-6	49	31
24	Superior frontal gyrus	Frontoparietal	8	51	30
25	Middle frontal gyrus	Default mode	-6	54	-7
26	Middle frontal gyrus	Default mode	7	52	-7
27	Gyrus rectus	Default mode	-6	37	-18
28	Gyrus rectus	Default mode	7	36	-18
29	Median cingulate and paracingulate gyri	Salience	-6	-15	42
30	Median cingulate and paracingulate gyri	Salience	7	-9	40
31	Hippocampus	Subcortical	-26	-21	-10
32	Hippocampus	Subcortical	28	-20	-10
33	Parahippocampal gyrus	Default mode	-22	-16	-21
34	Parahippocampal gyrus	Default mode	24	-15	-20
35	Amygdala	Subcortical	-24	-1	-17
36	Amygdala	Subcortical	26	1	-18

37	Calcarine fissure and surrounding cortex	Visual	-8	-79	6
38	Calcarine fissure and surrounding cortex	Visual	15	-73	9
39	Cuneus	Visual	-7	-80	27
40	Cuneus	Visual	13	-79	28
41	Lingual gyrus	Visual	-16	-68	-5
42	Lingual gyrus	Visual	15	-67	-4
43	Superior occipital gyrus	Visual	-18	-84	28
44	Superior occipital gyrus	Visual	23	-81	31
45	Middle occipital gyrus	Visual	-33	-81	16
46	Middle occipital gyrus	Visual	36	-80	19
47	Inferior occipital gyrus	Visual	-37	-78	-8
48	Inferior occipital gyrus	Visual	37	-82	-8
49	Fusiform gyrus	Visual	-32	-40	-20
50	Fusiform gyrus	Visual	33	-39	-20
51	Postcentral gyrus	Sensorimotor	-43	-23	49
52	Postcentral gyrus	Sensorimotor	40	-25	53
53	Superior parietal gyrus	Salience	-24	-60	59
54	Superior parietal gyrus	Salience	25	-59	62
55	Inferior parietal gyrus	Frontoparietal	-44	-46	47
56	Inferior parietal gyrus	Frontoparietal	45	-46	50
57	Supramarginal gyrus	Salience	-57	-34	30
58	Supramarginal gyrus	Salience	57	-32	34
59	Angular gyrus	Default mode	-45	-61	36
60	Angular gyrus	Default mode	45	-60	39
61	Precuneus	Default mode	-8	-56	48
62	Precuneus	Default mode	9	-56	44
63	Paracentral lobule	Sensorimotor	-9	-25	70
64	Paracentral lobule	Sensorimotor	6	-32	68
65	Caudate nucleus	Subcortical	-12	11	9
66	Caudate nucleus	Subcortical	14	12	9
67	Lenticular nucleus	Subcortical	-25	4	2
68	Lenticular nucleus	Subcortical	27	5	2
69	Lenticular nucleus	Subcortical	-19	0	0
70	Lenticular nucleus	Subcortical	20	0	0
71	Thalamus	Subcortical	-12	-18	8
72	Thalamus	Subcortical	12	-18	8
73	Heschl gyrus	Auditory	-43	-19	10
74	Heschl gyrus	Auditory	45	-17	10
75	Superior temporal gyrus	Auditory	-54	-21	7
76	Superior temporal gyrus	Auditory	57	-22	7
77	Temporal pole: superior temporal gyrus	Auditory	-41	15	-20
78	Temporal pole: superior temporal gyrus	Auditory	47	15	-17
79	Middle temporal gyrus	Auditory	-57	-34	-2
80	Middle temporal gyrus	Auditory	56	-37	-1
81	Temporal pole: middle temporal gyrus	Default mode	-37	15	-34
82	Temporal pole: middle temporal gyrus	Default mode	43	15	-32
83	Inferior temporal gyrus	Frontoparietal	-51	-28	-23
84	Inferior temporal gyrus	Frontoparietal	53	-31	-22
85	Insula	Salience	-35	14	-4
86	Insula	Salience	36	15	-5
87	Insula	Sensorimotor	-39	-9	0
88	Insula	Sensorimotor	39	-10	2
89	Parietal operculum	Sensorimotor	-52	-17	16
90	Parietal operculum	Sensorimotor	53	-16	16
91	Ant. Cingulate ctx	Default mode	-4	37	16

92	Ant. Cingulate ctx	Default mode	3	36	16
93	Perigenual ant. Cingulate ctx	Default mode	-5	40	-1
94	Perigenual ant. Cingulate ctx	Default mode	4	40	-1
95	Dorsal post. Cingulate ctx	Default mode	-3	-31	35
96	Dorsal post. Cingulate ctx	Default mode	2	-29	36
97	Ventral post. Cingulate ctx	Default mode	-5	-56	17
98	Ventral post. Cingulate ctx	Default mode	4	-54	19

Table A.1: 98 regions of interest (ROIs) of the brain and their functional system affiliation, as found in the AAL atlas (list obtained from [37]). The coordinates of each node in the Montreal Neurological Institute and Hospital (MNI) space are given by the columns x, y, and z.

Appendix B

Thresholding function

In order to convert dense functional connectivity matrices into sparse ones, we use a thresholding function. Meunier et al. [26] used a common practice of specifying a certain threshold value ν to determine the sparsity of the adjacency matrices. To create an adjacency matrix from a wavelet correlation matrix, element a_{ij} is then set to 1 if the absolute value of the wavelet correlation between nodes i and j exceeds ν, and 0 otherwise. The negative correlations in the wavelet correlation matrix are taken to be their absolute value, rather than setting the elements to 0. The value of ν in Meunier et al. is chosen so as to satisfy certain objectives, for instance to be small enough so that the graphs are dense enough to form a fully connected graph. In this context, a connected graph means one with a 'giant component'[14].

Given that our networks are a similar size to the ones presented in Meunier et al., ν is similarly chosen such that the number of edges in the network after the thresholding value has been used is between 100 and 400. Therefore, after applying this thresholding technique to the subject data, the resulting networks have a mean edge density between 0.02 and 0.08. We make a final note that the resulting graphs are not necessarily connected in the sense that there exists a path from every node to all other nodes.

---

[14]See Bollobas for further discussion [74].

Appendix C

Balanced approaches

In this appendix, we present two balanced approaches that aim to provide information at a nodal and entire network level, supplementing the metrics presented in Chapter 4.

C.1   Hamming-Ipsen-Mikhailov (HIM)

The Hamming-Ipsen-Mikhailov (HIM) distance, as introduced by Jurman et al. [64], allows the user to decide how much to focus on the global or local information. By combining the Hamming distance, a local measure, and the Ipsen-Mikhailov distance, a global measure, we are able to capture information at both levels.

Definition C.1.1. The *Hamming-Ipsen-Mikhailov distance* is defined by

$$d_{\text{HIM}}^{\eta} = \frac{1}{\sqrt{1+\eta}}\sqrt{\text{IM}^2 + \eta\text{H}^2}.$$

For our analysis we take the natural choice for the combination factor, $\eta = 1$, allowing for an equal contribution from the Hamming and Ipsen-Mikhailov metrics. The normalisation factor $\sqrt{1+\eta}$ ensures that the HIM distance between two graphs falls between 0, for identical networks, and 1, for the comparison of a complete graph and an empty graph.

In Figure C.1, the HIM distance between two networks representing time windows 1 and 2 for the mean of all subjects has been plotted as a function of η. We note here that at $\eta = 0$, the HIM distance is simply the Ipsen-Mikhailov distance but as η tends to infinity, the HIM distance tends to the Hamming distance.

When we apply the Hamming-Ipsen-Mikhailov metric to our brain networks, the results are very similar to the distances from the Ipsen-Mikhailov metric. This comparison can be seen in Figure C.2. This suggests that the global changes of the
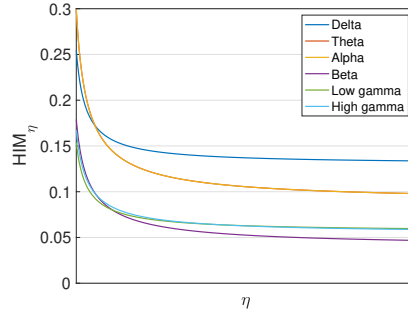
Figure C.1: The Hamming-Ipsen-Mikhailov (HIM) distance between networks representing time windows 1 and 2 for the mean of all subjects for $\eta \in [0, \infty)$.

graphs structures are driving the changes between networks, and thus we are unable to discover further insights through this balanced approach.

(a) Ipsen-Mikhailov

(b) Hamming-Ipsen-Mikhailov
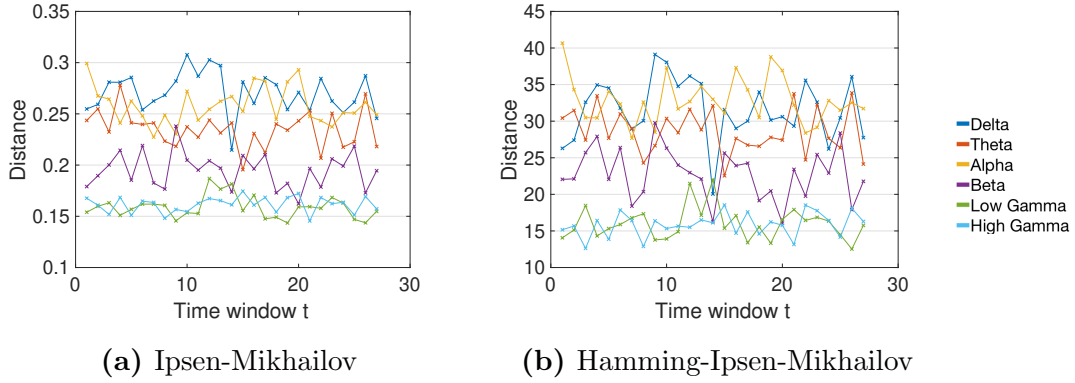
Figure C.2: Global distance metrics for the mean of all subjects, measured between networks representing time window 1 and time window t $(t = 2, 3, \ldots, 28)$.

66

C.2 Polynomial approach

The polynomial approach uses powers of the adjacency matrix A^k to calculate a new metric. Topologically speaking, the element A_{ij}^k represents the number of paths that start at node i and finish at node j with exactly k steps in between. By also noting the eigenvalue decomposition of the adjacency matrix, $A = V\Lambda_A V^T$, we are able to define its associated polynomial

$$\begin{aligned} \mathcal{P}(A) &= A + \frac{1}{(N-1)^\alpha}A^2 + \frac{1}{(N-1)^{2\alpha}}A^3 + \ldots + \frac{1}{(N-1)^{(K-1)\alpha}}A^K \\ &= V\left[\Lambda_A + \frac{1}{(N-1)^\alpha}\Lambda_A^2 + \frac{1}{(N-1)^{2\alpha}}\Lambda_A^3 + \ldots + \frac{1}{(N-1)^{(K-1)\alpha}}\Lambda_A^K\right]V^T \\ &= VZV^T, \end{aligned}$$

where

$$Z = \sum_{i=1}^K \frac{\Lambda_A^i}{(N-1)^{(i-1)\alpha}}.$$

The weighting factor α enables us to adjust whether minor changes in larger or smaller neighbourhoods have a larger effect on the overall distance. This polynomial can be used to define a polynomial distance.

Definition C.2.1. The *polynomial distance* between two graphs of N nodes, G and $\bar{G}$, with corresponding adjacency matrices A and $\bar{A}$, is calculated as

$$d_{\text{poly}}(G, \bar{G}) = \frac{1}{N^2}||\mathcal{P}(G) - \mathcal{P}(\bar{G})||_{2,2},$$

where

$$||M_1 - M_2||_{2,2} = \left(\sum_{i,j}|M_{i,j}^1 - M_{i,j}^2|^2\right)^{\frac{1}{2}}.$$

The polynomial approach captures information at a neighbourhood level, aiming to process how changes at node level affect the area around it. In Figure C.3 we compare the distances of the polynomial approach with those of the Hamming distance for the mean across 30 subjects. It can be seen that both metrics discover very similar distances between networks of each frequency band. In this particular case, the polynomial approach does not provide us with further insight into the networks transformations.

(a) Hamming
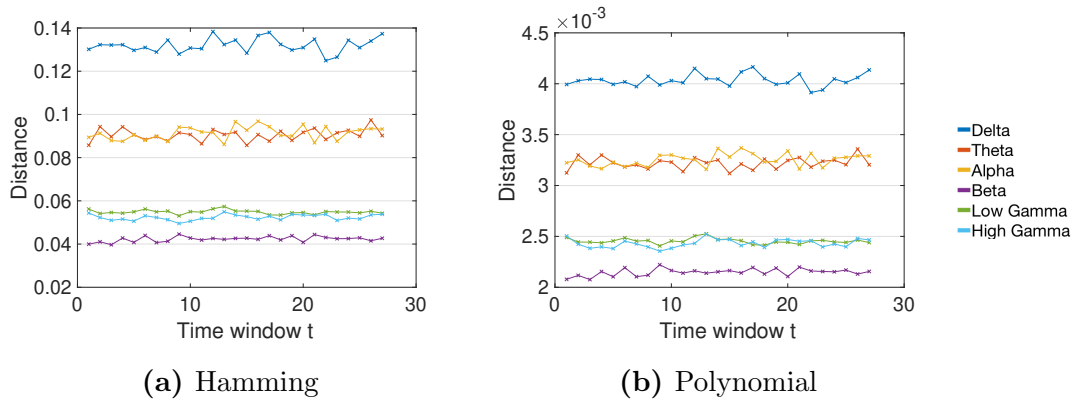
(b) Polynomial

Figure C.3: The mean Hamming and Polynomial distances across all subjects between networks representing time window 1 and time window t ($t = 2, 3, \ldots, 28$). For the polynomial distance $\alpha = 0.9$ and $K = 20$.

Appendix D

Statistical results

Static modular analysis of frequency bands

Frequency band 1	Frequency band 2	T-value	p-tukey
Alpha	Beta	-0.1572	0.9000
Alpha	Delta	2.1384	0.2692
Alpha	High gamma	13.10	0.0010
Alpha	Low gamma	8.563	0.0010
Alpha	Theta	0.1524	0.9000
Beta	Delta	2.296	0.1978
Beta	High gamma	13.26	0.0010
Beta	Low gamma	8.721	0.0010
Beta	Theta	0.3097	0.9000
Delta	High gamma	10.96	0.0010
Delta	Low gamma	6.425	0.0010
Delta	Theta	-1.986	0.3520
High gamma	Low gamma	-4.538	0.0010
High gamma	Theta	-12.95	0.0010
Low gamma	Theta	-8.411	0.0010

Table D.1: Tukey HSD test results for comparing modularity of networks of different frequency bands: p-tukey values for the pairwise comparison of the mean modularity of networks for all six frequency bands.

Frequency band 1	Frequency band 2	T-value	p-tukey
Alpha	Beta	0.1930	0.9000
Alpha	Delta	4.193	0.0010
Alpha	High gamma	22.59	0.0010
Alpha	Low gamma	9.696	0.0010
Alpha	Theta	3.575	0.0047
Beta	Delta	4.000	0.0010
Beta	High gamma	22.40	0.0010
Beta	Low gamma	9.503	0.0010
Beta	Theta	3.382	0.9437
Delta	High gamma	18.40	0.0010
Delta	Low gamma	5.503	0.0010
Delta	Theta	-0.619	0.9000
High gamma	Low gamma	-12.90	0.0010
High gamma	Theta	-19.02	0.0010
Low gamma	Theta	-6.121	0.0010

Table D.2: Tukey HSD test results for NMI: p-tukey values for the pairwise comparison of the mean NMI values for all six frequency bands.

Male vs female statistical results

Frequency band	p-value	Critical value
Delta	0.0204	0.0083
Theta	0.0366	0.0167
Alpha	0.1002	0.0250
Beta	0.1343	0.0333
Low gamma	0.3877	0.0417
High gamma	0.5679	0.0500

Table D.3: Permutation test results for modularity: FDR corrected p-values for the mean male vs female modularity with a q-value of 5%.

Frequency band	p-value	Critical value
Delta	0.162	0.0167
Theta	0.123	0.0083
Alpha	0.467	0.0500
Beta	0.216	0.0250
Low gamma	0.416	0.0417
High gamma	0.225	0.0333

Table D.4: Permutation test results for NMI: FDR corrected p-values for the mean male vs female NMI values with a q-value of 5%.

Frequency band	Recruitment	Integration	Flexibility	Promiscuity
Delta	0.401	0.4069	0.9922	0.6472
Theta	0.1197	0.1052	0.7987	0.4794
Alpha	0.7774	0.8982	0.3589	0.2850
Beta	0.2524	0.3854	0.5540	0.1437
Low gamma	0.2988	0.1806	0.6849	0.9977
High gamma	0.5699	0.7471	0.2700	0.2904

Table D.5: Node level dynamic metrics permutation test results: p-values for the mean male vs female recruitment, integration, flexibility, and promiscuity.

Functional system	Delta	Theta	Alpha	Beta	Low gamma	High gamma
Auditory	0.1727	0.6204	0.496	0.9843	0.2152	0.0915
Default mode	0.2073	0.3189	0.5215	0.4623	0.8024	0.7402
Frontoparietal	0.3158	0.0866	0.8888	0.1683	0.0514	0.2908
Salience	0.7943	0.1527	0.4085	0.7660	0.5454	0.4956
Sensorimotor	0.2361	0.3539	0.5470	0.8113	0.1380	0.0491
Subcortical	0.8006	0.0918	0.8490	0.2353	0.7112	0.1649
Visual	0.5132	0.4878	0.1372	0.5802	0.5078	0.3177

Table D.6: System level flexibility permutation test results: p-values for the mean male vs female flexibility.

Functional system	Delta	Theta	Alpha	Beta	Low gamma	High gamma
Auditory	0.1400	0.8302	0.324	0.3899	0.4057	0.0997
Default mode	0.4818	0.5130	0.3447	0.1173	0.7684	0.8952
Frontoparietal	0.2254	0.0705	0.9756	0.0580	0.0344	0.4263
Salience	0.7760	0.5854	0.4096	0.9122	0.7213	0.3807
Sensorimotor	0.3000	0.2327	0.5405	0.6747	0.4242	0.0622
Subcortical	0.6510	0.0414	0.8525	0.1518	0.9656	0.2673
Visual	0.7298	0.8172	0.1656	0.9005	0.7134	0.3544

Table D.7: System level promiscuity permutation test results: p-values for the mean male vs female promiscuity.

Functional system	Auditory	Default mode	Frontoparietal	Salience	Sensorimotor	Subcortical	Visual
Auditory	0.3605	0.9622	0.6774	0.8762	0.2609	0.495	0.2789
Default mode	0.9622	0.171	0.0848	0.7131	0.3131	0.3287	0.4744
Frontoparietal	0.6774	0.0848	0.4647	0.3001	0.0872	0.3921	0.4458
Salience	0.8762	0.7131	0.3001	0.8319	0.3298	0.8851	0.0131
Sensorimotor	0.2609	0.3131	0.0872	0.3298	0.1008	0.1118	0.0641
Subcortical	0.495	0.3287	0.3921	0.8851	0.1118	0.59	0.0547
Visual	0.2789	0.4744	0.4458	0.0131	0.0641	0.0547	0.5294

Table D.8: System level recruitment and integration permutation test results: p-values for the mean male vs female recruitment and integration values for the delta frequency band. The diagonal elements of the table represent the recruitment of the corresponding system and the off-diagonal elements represent the integration between the two corresponding systems.

Functional system	Auditory	Default mode	Frontoparietal	Salience	Sensorimotor	Subcortical	Visual
Auditory	0.9157	0.3149	0.9701	0.2631	0.1599	0.8097	0.1797
Default mode	0.3149	0.5774	0.1765	0.4481	0.9951	0.8981	0.7858
Frontoparietal	0.9701	0.1765	0.3306	0.9279	0.2236	0.5988	0.8717
Salience	0.2631	0.4481	0.9279	0.411	0.5404	0.0642	0.001
Sensorimotor	0.1599	0.9951	0.2236	0.5404	0.424	0.283	0.0076
Subcortical	0.8097	0.8981	0.5988	0.0642	0.283	0.6871	0.7991
Visual	0.1797	0.7858	0.8717	0.001	0.0076	0.7991	0.2679

Table D.9: System level recruitment and integration permutation test results: p-values for the mean male vs female recruitment and integration values for the theta frequency band. The diagonal elements of the table represent the recruitment of the corresponding system and the off-diagonal elements represent the integration between the two corresponding systems.

Functional system	Auditory	Default mode	Frontoparietal	Salience	Sensorimotor	Subcortical	Visual
Auditory	0.0923	0.4378	0.9604	0.2765	0.6999	0.1769	0.1281
Default mode	0.4378	0.6122	0.7301	0.3223	0.506	0.5269	0.9884
Frontoparietal	0.9604	0.7301	0.8557	0.8227	0.1152	0.9076	0.2608
Salience	0.2765	0.3223	0.8227	0.1448	0.6413	0.1519	0.0705
Sensorimotor	0.6999	0.506	0.1152	0.6413	0.3074	0.7527	0.0483
Subcortical	0.1769	0.5269	0.9076	0.1519	0.7527	0.883	0.9568
Visual	0.1281	0.9884	0.2608	0.0705	0.0483	0.9568	0.5536

Table D.10: System level recruitment and integration permutation test results: p-values for the mean male vs female recruitment and integration values for the alpha frequency band. The diagonal elements of the table represent the recruitment of the corresponding system and the off-diagonal elements represent the integration between the two corresponding systems.

Functional system	Auditory	Default mode	Frontoparietal	Salience	Sensorimotor	Subcortical	Visual
Auditory	0.5565	0.9805	0.5617	0.9292	0.3209	0.6277	0.4262
Default mode	0.9805	0.6283	0.2587	0.3431	0.799	0.692	0.4814
Frontoparietal	0.5617	0.2587	0.5888	0.6055	0.8283	0.5212	0.6021
Salience	0.9292	0.3431	0.6055	0.935	0.7731	0.4939	0.062
Sensorimotor	0.3209	0.799	0.8283	0.7731	0.3023	0.5563	0.3696
Subcortical	0.6277	0.692	0.5212	0.4939	0.5563	0.8795	0.6987
Visual	0.4262	0.4814	0.6021	0.062	0.3696	0.6987	0.9947

Table D.11: System level recruitment and integration permutation test results: p-values for the mean male vs female recruitment and integration values for the beta frequency band. The diagonal elements of the table represent the recruitment of the corresponding system and the off-diagonal elements represent the integration between the two corresponding systems.

Functional system	Auditory	Default mode	Frontoparietal	Salience	Sensorimotor	Subcortical	Visual
Auditory	0.4019	0.3891	0.3526	0.4763	0.365	0.6862	0.4563
Default mode	0.3891	0.8635	0.5111	0.8685	0.5756	0.2815	0.1851
Frontoparietal	0.3526	0.5111	0.8746	0.915	0.2385	0.2127	0.3389
Salience	0.4763	0.8685	0.915	0.568	0.5404	0.3133	0.9163
Sensorimotor	0.365	0.5756	0.2385	0.5404	0.3981	0.7673	0.3292
Subcortical	0.6862	0.2815	0.2127	0.3133	0.7673	0.7155	0.5374
Visual	0.4563	0.1851	0.3389	0.9163	0.3292	0.5374	0.1875

Table D.12: System level recruitment and integration permutation test results: p-values for the mean male vs female recruitment and integration values for the low gamma frequency band. The diagonal elements of the table represent the recruitment of the corresponding system and the off-diagonal elements represent the integration between the two corresponding systems.

Functional system	Auditory	Default mode	Frontoparietal	Salience	Sensorimotor	Subcortical	Visual
Auditory	0.6707	0.412	0.6623	0.3123	0.6548	0.5856	0.0448
Default mode	0.412	0.6271	0.4583	0.8053	0.2504	0.5948	0.1725
Frontoparietal	0.6623	0.4583	0.2633	0.774	0.4221	0.4049	0.2015
Salience	0.3123	0.8053	0.774	0.3746	0.4273	0.7764	0.4958
Sensorimotor	0.6548	0.2504	0.4221	0.4273	0.3128	0.8105	0.074
Subcortical	0.5856	0.5948	0.4049	0.7764	0.8105	0.567	0.5084
Visual	0.0448	0.1725	0.2015	0.4958	0.074	0.5084	0.0641

Table D.13: System level recruitment and integration permutation test results: p-values for the mean male vs female recruitment and integration values for the high gamma frequency band. The diagonal elements of the table represent the recruitment of the corresponding system and the off-diagonal elements represent the integration between the two corresponding systems.

Distance Metric	Delta	Theta	Alpha	Beta	Low gamma	High gamma
Hamming	< 0.0001	< 0.0001	< 0.0001	0.0003	< 0.0001	< 0.0001
Jaccard	0.0853	0.0905	0.0027	0.0002	< 0.0001	< 0.0001
Spanning tree	0.3257	0.0013	< 0.0001	0.1908	0.0034	< 0.0001
Ipsen-Mikhailov	0.0958	0.0027	0.0004	0.0688	< 0.0001	< 0.0001
Hamming-Ipsen-Mikhailov	0.0076	0.0100	0.0002	0.0770	< 0.0001	< 0.0001
Polynomial	< 0.0001	< 0.0001	< 0.0001	0.0023	< 0.0001	< 0.0001
Centrality	0.0207	0.5383	0.0047	< 0.0001	< 0.0001	< 0.0001
Heat spectral wavelet	0.0111	0.0007	< 0.0001	< 0.0001	< 0.0001	< 0.0001

Table D.14: T-test results for means of all distance metrics: p-values for the mean male vs female distances from time window 1 to $t = 2, \ldots, 28$ as calculated by the metrics presented in Chapter 4.

Distance metric	Delta	Theta	Alpha	Beta	Low gamma	High gamma
Hamming	< 0.0001	< 0.0001	< 0.0001	0.0004	< 0.0001	< 0.0001
Jaccard	0.0848	0.0903	0.0024	0.0004	< 0.0001	< 0.0001
Spanning tree	0.3256	0.0009	< 0.0001	0.1906	0.0032	< 0.0001
Ipsen-Mikhailov	0.0959	0.0026	0.0008	0.0689	< 0.0001	< 0.0001
Hamming-Ipsen-Mikhailov	0.0076	0.0091	0.0003	0.0760	< 0.0001	< 0.0001
Polynomial	< 0.0001	< 0.0001	< 0.0001	0.0030	< 0.0001	< 0.0001
Centrality	0.0200	0.5335	0.0054	< 0.0001	< 0.0001	< 0.0001
Heat spectral wavelet	0.0120	0.0013	< 0.0001	< 0.0001	< 0.0001	< 0.0001

Table D.15: Permutation test results for means of all distance metrics: p-values for the mean male vs female distances from time window 1 to $t = 2, \ldots, 28$ as calculated by the metrics presented in Chapter 4.

Distance metric	Delta	Theta	Alpha	Beta	Low gamma	High gamma
Hamming	0.9131	0.5181	0.5024	0.6317	0.4148	0.1561
Jaccard	0.7764	0.8343	0.6125	0.7863	0.2942	0.1218
Spanning tree	0.8612	0.0381	0.1591	0.5113	0.6849	0.2700
Ipsen-Mikhailov	0.9760	0.0373	0.4208	0.5113	0.2952	0.9577
Hamming-Ipsen-Mikhailov	0.9727	0.0408	0.3928	0.4806	0.3087	0.9089
Polynomial	0.9586	0.5593	0.5121	0.7200	0.3159	0.0487
Centrality	0.7930	0.0577	0.4244	0.6795	0.2923	0.3796
Heat spectral wavelet	0.8609	0.3898	0.7144	0.3229	0.1539	0.9311

Table D.16: Levene's test results for variances of all distance metrics: p-values for the variance of male vs female distances from time window 1 to $t = 2, \ldots, 28$ as calculated by the metrics presented in Chapter 4.